IMAGING THE FAULT RUPTURES OF THE GREAT 2012 INDIAN OCEAN INTRAPLATE EARTHQUAKES FROM BACK-PROJECTION OF TELESEISMIC P-WAVES

by

Kevin Brian Kwong

A thesis submitted to the faculty of
The University of Utah
in partial fulfillment of the requirements for the degree of

Master of Science

in

Geophysics

Department of Geology and Geophysics

The University of Utah

December 2013

The University of Utah Graduate School

STATEMENT OF THESIS APPROVAL

The thesis of **Kevin Brian Kwong**

has been approved by the following supervisory committee members:

Keith Koper	, Chair	**10/23/2013** Date Approved
Kristine L. Pankow	, Member	**10/23/2013** Date Approved
Michael S. Thorne	, Member	**10/23/2013** Date Approved

and by **John M. Bartley** , Chair/Dean of

the Department/College/School of **Geology and Geophysics**

and by David B. Kieda, Dean of The Graduate School.

ABSTRACT

P-wave observations from seismic stations in Europe and Japan were used to track the short-period energy release of the April 11, 2012 M_w 8.7 mainshock and M_w 8.2 aftershock that occurred in the Indian Ocean. Both were intraplate strike-slip events that ruptured in the region of a diffuse plate boundary within the Indo-Australian plate. We performed back-projection analyses using 85 vertical component broadband stations in Europe and 72 F-net stations and ~760 Hi-net stations in Japan. The high-passed back-projection images from the different arrays show similar trends in the short-period energy release. The locations of short-period rupture coincided with the complex aftershock distribution which suggests rupture on multiple conjugate fault planes. Back-projection results for the M_w 8.2 aftershock suggest bilateral rupture on an NNE-SSW fault plane with dominant energy located to the NNE. Seven large aftershocks were used to retrieve travel-time correction values to be interpolated over the grid region. The new back-projection results of the European array using the empirical aftershock corrections aligned the mainshock subevents and projected into linear fault trace features. We further investigate the mainshock fault geometry and rupture properties by back-projecting synthetic seismograms modeled from four finite fault slip models. The geometry of the fault models differ between the primary fault being conjugate or orthogonal or sub-parallel to the secondary fault. One of the fault models included a super-shear rupture parameter. Out of the four synthetic derived images, the orthogonal fault model, is the

most similar to the data-derived back-projection images. We conclude that the mainshock ruptured four conjugate faults; two WNW-ESE subparallel faults, one fault orthogonal to the main fault, and a possible WNW-ESE fault to the far west.

To my grandmother Yuet Ngor Chu Chan

TABLE OF CONTENTS

LIST OF FIGURES

ACKNOWLEDGEMENTS

I am most grateful to my advisor Dr. Keith Koper for his guidance and support. I am also grateful to Dr. Michael Thorne and Dr. Kris Pankow for their support and helpful comments. I would like to thank my colleague and friend Oner Sufri for his advice and guidance.

I received generous funding and support from the University of Utah, Department of Geology and Geophysics and the University of Utah Seismograph Stations.

CHAPTER 1

INTRODUCTION

1.1 The Massive Indian Ocean Strike-Slip Earthquakes of 2012

On April 11th 2012, the occurrence of two magnitude 8+ earthquakes beneath the Indian Ocean, 100-200 km off the west coast of northern Sumatra, was unprecedented. The estimated seismic moment magnitude of the mainshock (M_w 8.6) and a large aftershock (M_w 8.2) occurring 2 hours later were of significant size, unusual, and unexpected in the region. These great events ruptured in the northern Wharton Basin away from significant plate boundaries, thereby revealing themselves as noteworthy oceanic intraplate earthquakes. Fortunately, as large as the mainshock was, a significant tsunami was not generated. This is due to the fact that the fault mechanism of the mainshock was strike-slip as opposed to a thrust mechanism occurring in or around a subduction zone, such as the disastrous 2004 M_w 9.1 Sumatra-Andaman earthquake. Strike-slip events involve a lateral displacement of water and thus do not generate the same tsunami potential as would result from the vertical displacement of water from subduction zone thrust faulting events.

The strike-slip fault plane solutions determined from moment tensor inversions for the mainshock (http://www.globalcmt.org) and following aftershocks are consistent with

the previously observed occurrence of left-lateral strike-slip earthquakes occurring in the Wharton Basin. Earlier in the year, a significant strike-slip earthquake (M_w 7.2) occurred near the April mainshock epicenter (January 10, 2012). Until recently, it did not seem likely that a nonsubduction related event larger than a magnitude 8 could occur in the Indian Ocean. The M_w 8.6 mainshock is the largest seismically recorded intraplate earthquake in history and is a contender for the largest strike-slip earthquake ever recorded, along with the 1950 Assam earthquake in Tibet (M_s 8.6). However, source details are not well-constrained for the Assam event because of the small number of seismic observations.

Although the massive strike-slip sequence came as a surprise, it illustrates the ongoing changes that are driving the breakup of the Indo-Australian plate to the eventual formation of a new plate boundary. Significant evidence from earthquakes occurring in the diffuse boundary between the rigid Indian and Australian plates (northern Wharton Basin) suggests a region of intraplate deformation with prominent left-lateral shear fracture zones striking NNE-SSW [*Delescluse and Chamot-Rooke*, 2007].

1.2 Tectonics of the Indian Ocean

The most seismically active oceanic plate interior on Earth resides in the Indian Ocean [*Bergman and Solomon*, 1985]. The active seismicity illustrates the complex diffuse deformation in the region that results from the interplay of the Indo-Australian plate colliding with Eurasia and subducting along the Sunda-Arc (Figure 1). It is important to note that India and Australia are not contained in a single, rigid tectonic

plate but instead, there are models delineating the boundary of diffusive internal deformation proposed within the Indo-Australian plate.

As mentioned earlier, the M_w 8.6 mainshock focal mechanism had a NNE-SSW striking plane (Figure 1) that is consistent with the intraplate deformation within the Indo-Australian plate. The Ninety-East Ridge plays an important role as a kinematic boundary between India and Australia, and is known to be a complex zone of deformation with a history of significant seismicity. The northern portion of the ridge is, however, much more seismically active than the southern portion. Focal mechanism solutions of large earthquakes for this area propose left-lateral strike-slip motion striking roughly N-S along the ridge and compressive motion across the ridge striking roughly E-W. The historical earthquakes in this region provide an important constraint on the geographical extent and kinematics of the diffuse plate boundary. The region of diffuse plate convergence within the Indo-Australian plate extends far across the Ninety-East Ridge. The distributed zone of intraplate deformation meets with three component subplates: the Indian, Australian, and Capricorn; making up the composite Indo-Australian plate [*Royer and Gordon*, 1997].

In our study area, east of the Ninety-East Ridge, the northern Wharton Basin is cut by several parallel N-S trending fossil fracture zones. It is thought that the 2000 June 4th and 18th M_w 7.9 earthquakes with left-lateral strike-slip ruptures reactivated the N-S fossil transform faults. Both of the June 2000 earthquakes, like the April 2012 earthquakes, were unexpected and were of significant size. These recent large oceanic intraplate earthquakes add new critical information about the present-day complex deformation in the Indian Ocean.

1.3 Early Source Observations

The 2012 M_w 8.6 and 8.2 Indian Ocean earthquakes certainly defied our expectations of the potential size of an oceanic strike-slip earthquake. Aside from the surprising size, the observed rupture complexity of the mainshock is unlike any previous rupture seen in modern seismology. The early aftershock distribution was extremely complex and suggested that the mainshock likely ruptured on several different faults. Since the earthquakes occurred in a remote region, severely limiting the observations from near-source networks of seismic and geodetic instruments, teleseismic observations have provided the most important space-time history constraint of the rupture process.

Early finite-fault inversions using teleseismic data preferred a single fault model striking NNE or SSW [*Hayes*, 2012; *Shao et al*., 2012]. However, back-projection analyses using teleseismic P-waves from different groups showed a complex space-time history of the rupture in agreement with the aftershock distribution. The use of back-projection of short-period seismic waveforms to image the rupture process of large earthquakes has become increasingly popular since Ishii *et al.* [2005] introduced the method for the 2004 M_w 9.1 Sumatra-Andaman mega-thrust rupture.

The limitations of short-period back-projections include insensitivity to the relative magnitude of fault slip and thus an inability to resolve the seismic moment of the fault rupture. The benefits of the back-projection method include the ability to resolve the short-period seismic radiation that is sensitive to slip rate variations instead of total slip. By tracking the short-period radiation of the complex 11 April 2012 mainshock, coherent bursts of seismic energy are located on multiple potential fault planes. The back-projection results of the mainshock and also the M_w 8.2 aftershock have been roughly

consistent across different groups [*Hutko* 2012; *Kiser et al*., 2012; *Meng et al*., 2012; *Satriano et al*., 2012; *Wang et al*., 2012; *Yue et al*., 2012; *Zhang et al*., 2012]. A discrepancy between the back-projection models and the finite-fault models of the mainshock involves the former preferring an E-W main fault rupture and the later an N-S main fault rupture.

The constraints from back-projection and aftershock locations helped parameterize an updated mainshock finite-fault model (upgraded to M_w 8.7) that prefers multiple faults [*Yue et al*., 2012]. There is no fault model for the large aftershock because the mainshock surface waves obscured the incoming P and SH waves of the aftershock. The updated mainshock finite fault model preferred four primary subfaults that featured a triggered bilateral failure on a cross-cutting orthogonal fault.

1.4 Resolving Key Issues

There are several key issues that need to be addressed concerning the source properties of the two great 11 April 2012 events. The energy partitioning between subfaults in the finite fault inversion of the mainshock is an important issue that needs to be resolved. Inverted finite fault models show a discrepancy between the orientation of the main fault and the secondary fault. Yue *et al*. [2012] prefer an E-W trending main fault that is orthogonal or conjugate from the cross-cutting secondary fault. However, the updated finite fault model inversion result from Shao and Ji [2012] prefer an N-S trending main fault that is subparallel to the secondary fault.

The rupture velocity of the mainshock is another important issue that needs to be resolved. Wang *et al.* [2012] propose a supershear rupture model from short-period back-

projection constraints that showed fault segments rupturing as high as 5 km/s, exceeding the local S-wave velocity. In contrast, the short-period back-projection constraints from Meng *et al*. [2012] prefer a relatively low rupture speed with fault segments rupturing as low as ~2.5 km/s.

The rupture process of the large aftershock is compact and simple compared to the mainshock. The rupture duration of the aftershock is about half as long as the mainshock. Due to the difficulty inverting for an aftershock finite fault model, detailed source properties have yet to be resolved for this event.

In this study, we present our back-projection results of the two great 11 April 2012 Indian Ocean events. Our main motivation is to resolve the complex mainshock rupture properties by improving our back-projection method and provide reliable short-period rupture constraints. We will showcase the advantages and convenience of back-projection imaging in the case when the fault parameters are not well defined.

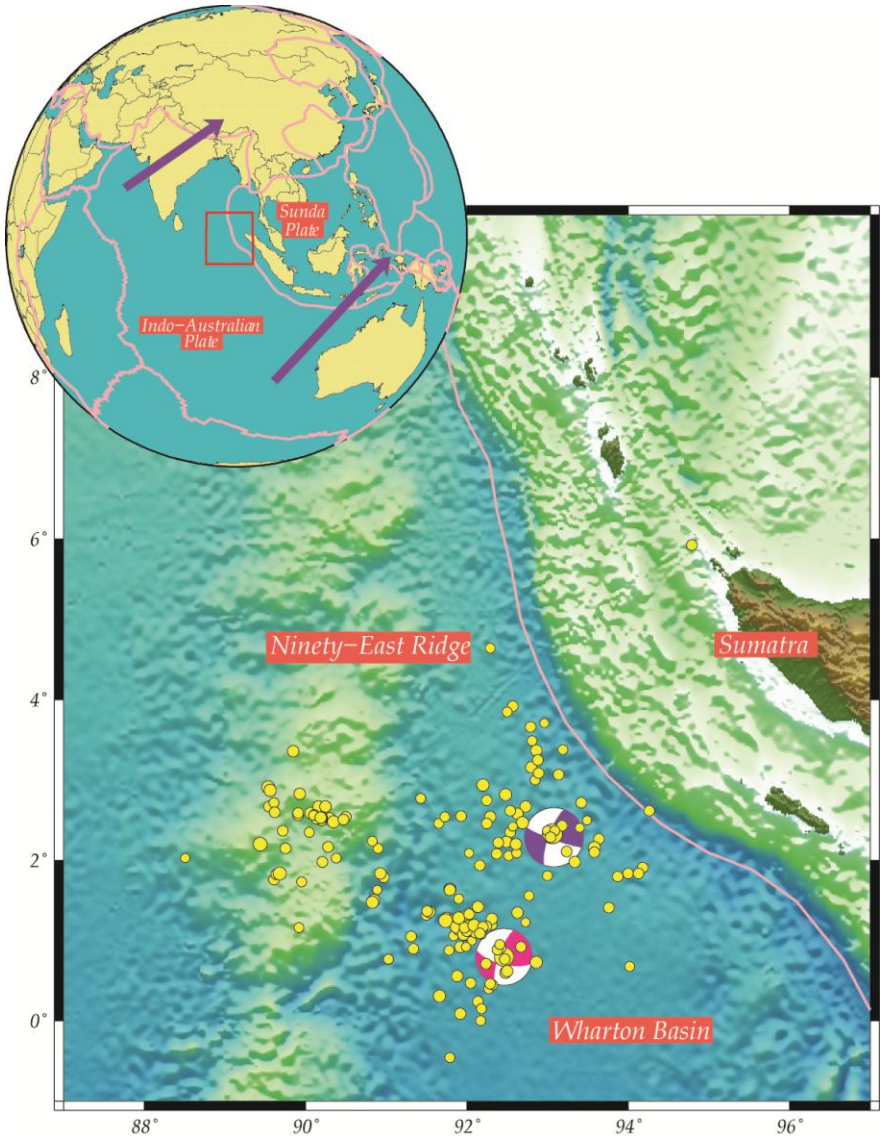

Figure 1. Study region. Red box indicates the area of the larger map where the April 11, 2012 Indian Ocean earthquakes occurred. Purple focal mechanism: M_w 8.7 mainshock. Pink focal mechanism: M_w 8.2 aftershock. Yellow circles indicate aftershock locations for the first day. Pink lines indicate plate boundary locations. Purple arrows indicate movement of the Indo-Australian plate with respect to the Sunda plate.

CHAPTER 2

THE BACK-PROJECTION METHOD

2.1 Application to Large Earthquakes

The increase of dense and large-aperture seismic network coverage around the Earth over the past decade has made back-projection studies one of the most exciting and useful techniques for studying the rupture properties of large earthquakes. The back-projection method uses an array of seismic stations to focus in on the desired beam direction and thus track the rupture process of an earthquake, an approach explored many years ago [e.g., *Spudich and Cranswich,* 1984]. However, it was not until the 2004 M_w 9.1 Sumatra-Andaman earthquake that the seismology community realized the possibilities of using a large-aperture array to track earthquake rupture processes at teleseismic distances [*Ishii et al*., 2005; *Krueger and Ohrnberger*, 2005].

Imaging the rupture process of an earthquake using the back-projection method is essentially an array-based approach to determine the location and amplitude of coherent high-frequency seismic radiation by stacking the seismic energy of an array at each grid point around the source region. A distinguishing feature of back-projection studies is that they determine rupture properties at shorter periods (~0.5-5s) than those used in traditional finite-fault source tomography inversion. The short-period P-wave

observations have an advantage in highlighting peak energy regions of the rupture more so than peak slip. Thus, the back-projection images are more sensitive to variations in slip-rate or slip-velocity, and provide unique but complimentary details of the fault rupture to traditional longer-period fault slip inversion models.

What makes back-projection study of large earthquakes popular is its simplicity and potential for rapid hazard analysis. Unlike finite fault models, the calculation of Green's functions is ignored and knowledge about the fault plane and moment tensor solution is not needed. The only *a priori* information required to perform back-projection analyses is a radial velocity model and the hypocentral location and origin time.

In a near-real-time environment that follows immediately after a significant earthquake, back-projection analyses can be computed within 30 minutes of the origin time. Within this time, detailed images about the short-period rupture propagation and areas of strong ground shaking in space and time can be relayed to the public to provide constraints on hazard analysis. Although back-projection imaging does not recover the total slip on a fault as do finite fault inversions, the computational time of back-projection is faster since inverting for a fault model can be more time consuming, especially if prior knowledge of the mainshock fault plane is not constrained. Another interesting feature of back-projection imaging is that a rough estimate of the rupture velocity can be inferred rapidly from the locations of local maximum peak energy. In the following sections, we will explain our back-projection method to image earthquake rupture that follows a similar procedure described in Xu *et al.* [2009].

2.2 Coherency of P-waves

The ability to resolve the earthquake rupture increases if the seismic array aperture is large and the frequency and similarity between waveforms is higher. Short-period waveforms are better able to resolve smaller features than long-period waveforms, but coherency degrades between waveforms faster at progressively shorter distances. Considering an array configuration, there is a tradeoff in needing coherency over a wide aperture versus the slowness resolution (or the accuracy of the measurement of the incoming wavefront direction and velocity). We prefer to use teleseismic arrays that are between 30°-95° distance from the source. In this distance range, the P-waves turn into the lower mantle with less interference of P-coda at regional distances (< 30°). At distances greater than 95°, the P-arrivals diffract around the core and the waveforms are no longer coherent with P-arrivals at shorter distances. The earthquake faulting mechanism provides the source-dependent coherency of P-waves, such that dip-slip earthquakes radiate P-wave energy further from nodal planes than strike-slip earthquakes and thus result in more similar waveforms.

2.3 Data Collection

We collect teleseismic P-wave data from networks of vertical component broadband seismometers located at distances 30°-95° from the mainshock epicenter. We experimented with using different teleseismic arrays of varying azimuthal distances from the mainshock. The robust results we present in this study used data from Japan and Europe. Seismic records in Japan were obtained from the National Research Institute for Earth Science and Disaster Prevention (NIED): F-net data from www.fnet.bosai.go.jp and

Hi-net data from www.hinet.bosai.go.jp. Seismic records from Europe were obtained from the Orpheus data center (www.orfeus-eu.org).

2.4 Travel-Time and Amplitude Corrections

In our back-projection procedure, we define a set of grid points around the earthquake fault region to locate potential sources of seismic radiation. The calculation of the predicted travel time from each grid point to a seismometer at a teleseismic distance needs to be accurate for the array beam to respond coherently. We calculate theoretical travel times from the 1D Earth model AK135 [*Kennett et al.*, 1995]. However, just using a radial Earth model alone is not accurate enough to predict the travel time and account for the 3D variations in Earth structure that causes travel time anomalies. To account for a more realistic 3D Earth structure, we determine an empirical set of travel time corrections for each station by aligning the first 10 s of the P-waves. Although this correction factor only takes into account the travel time from the mainshock hypocenter to the seismometer, we generally use this set of mainshock hypocenter correction factors for all grid points and assume that the travel time correction factors deviate slowly from the source location. In addition to correcting for travel time anomalies, we also correct for amplitude anomalies since the amplitude of the P-wave can vary upon several factors including, geometrical spreading, site effects, and radiation patterns.

There are several methods to align seismic traces. Our preferred method is the Multichannel Cross Correlation (MCCC) method of VanDecar and Crosson [1990]. This method computes the correlation function between all possible pairs of traces and uses a least squares estimation to derive arrival time picks for each trace. The traces are aligned

relative to a reference phase defined by the predictions of the AK135 model from a hypocentral estimate. In this study, we use the USGS National Earthquake Information Center (NEIC) hypocentral locations for our events. The MCCC alignment generates the cross-correlation coefficient, the time-shift value relative to the hypocentral location, and the normalized amplitude value calculated from the peak amplitude within the cross-correlated time window for each station.

2.5 Stacking Procedure

The last step in our back-projection procedure is stacking the aligned P-wave traces into a beam for each grid location. For this study, we discretize the source region by considering a 2D grid with no depth resolution according to the following geometry. We construct a grid (cell size 0.05°) extending from -1° to 5° in latitude and 88° to 95° in longitude. The depth of each grid node is fixed to 20 km for the mainshock and 25 km for the large aftershock. We use the MCCC-derived static corrections to normalize the amplitudes and time shift the seismograms to calculate the propagation from the station to each potential source location on our 3D grid using the AK135 model. Each grid point is a potential source location and we calculate the beam power for each point by stacking the seismograms aligned to the reference P phase and applying a tapered window function centered on a targeted time. Calculating the beam image against time makes the grid of potential source locations become four-dimensional (including latitude, longitude, and depth). We inspect the rupture process in time by calculating the beam power on every grid point starting 20 s before the origin time and shifting the tapered window by 1 s with a sliding window length of 10 s. The beam is calculated for the mainshock for a

total of 220 s and 140 s for the large aftershock. The robust back-projection images we report on are for data that are filtered from 0.5-2.0 Hz using a 4-pole Butterworth filter.

We used Nth root stacking, as it has shown to be effective in suppressing glitches and false alarm signals [*McFadden et al*., 1986]. The overall rupture images appear sharper and the spatial spread of the beam is more compact when using Nth root stacking versus linear stacking. We prefer to use fourth-root stacking; although higher order root stacking provides some improvement over the beam image, the differences decrease between higher orders. A potential significant bias of back-projection images arises from stacking in the time domain that is known to cause "swimming" artifacts. The time evolution of the beam image appears as if the energy is systematically traveling in the direction of the receiving array. Improved azimuthal coverage of the source can limit the bias in the "swimming" energy in a particular direction.

CHAPTER 3

BACK-PROJECTION RESULTS

3.1 P-waves from the European Array

The most robust back-projection results came from the observations of teleseismic P-waves recorded by a network of stations in and around Europe, which we refer to as our European array. For this array, we used vertical component recordings from a total of 85 broadband stations to compute back-projection images. The alignment of the P-waves recorded in Europe appears visually coherent for the M_w 8.7 mainshock and the M_w 8.2 aftershock (Figure 2).

We summarize our back-projection images for the mainshock and large aftershock by presenting a time integrated beam image of the rupture (Figure 3) and snapshots of the beam image for when there was significant changes in rupture propagation (Figures 4 and 5). The time integrated rupture image is produced by averaging over 11 time frame windows of the beam image. The amplitude of the beam power corresponding to the intensity of short-period energy release is plotted against time.

The obvious standout feature of the mainshock time integrated beam image (Figure 3) is that the locations of short-period energy have a direct correspondence to the locations of early aftershocks. The short-period rupture clearly overlays the complex early aftershock zone. As elaborated below, the aftershock locations reveal possible

cross-cutting and parallel fault orientations. The WNW-ESE trending aftershock cluster at the epicenter location suggests the main fault orientation. Lasting for about 40 s, the initial rupture stage of the mainshock showed a bilateral rupture with stronger radiation emitted from the western side of the main fault plane (Figure 4). The emergence of a distinct second rupture stage begins at about 57 s, showing a coherent subevent at the western side of the main fault. At about 68 s, north of this subevent, seismic radiation is emitted on a perpendicular aftershock zone.

After about 70 s, a third rupture stage emerges on a second WNW-ESE trending fault roughly parallel to the main fault and is approximately 150 km southwest of the epicenter. Including the large M_w 8.2 aftershock, a distinct group of aftershocks line up on this parallel fault plane. The rupture propagates to the WNW direction away from the M_w 8.2 aftershock location. The M_w 8.2 aftershock epicenter region and the ESE side of the fault did not appear to have any significant seismic radiation. Finally, a distinct fourth stage of rupture initiates at about 140 s emitting weak radiation but persists on a distinct cluster of aftershocks further west from the third rupture stage. Overall, the mainshock multistage rupture lasted for about 180 s. The four distinct stages of short-period energy release suggest that the mainshock triggered rupture on four fault planes. The fault orientation for the last rupture stage is the most ambiguous.

The short-period energy release of the M_w 8.2 aftershock is emitted over a compact region that lasted for about 80 s (Figure 5), about half as long as the mainshock. The strongest short period energy release is to the NNE of the epicenter lasting for about 22 s, and the remaining rupture seems to show weak energy release to the SSW, indicating that the rupture was bilateral on a single NNE or SSW fault plane.

3.2 P-waves from the F-net Array in Japan

We observe similar patterns of short-period energy release from P-waves recorded in Japan as documented for the P-waves recorded in Europe. The F-net array consists of a network of broadband stations distributed throughout Japan. The aperture of the F-net array is smaller and provides poorer resolution than the European array. Seventy-two vertical component recordings from the F-net network were used to back-project the mainshock and large aftershock (Figure 6). Figure 7 shows the time-integrated results, and snapshot images of the rupture are shown in Figures 8 and 9.

The initial short-period energy release does not indicate bilateral rupture as was determined with the European data. Although similar to the European results, strong seismic radiation is located on the western side of the main fault. After 40 s, we start to see energy release that could be rupture on the perpendicular fault. The energy that shows up at the location of the M_w 8.2 epicenter could possibly be an artifact. The following rupture stage on the third fault parallel to the main fault at around 100 s shows similar rupture propagation as the European results but is not as detailed and coherent. Although the fourth and last rupture segment after 140 s seems to show stronger radiation than the European results, the orientation of the fault is ambiguous.

The overall short-period energy release of the M_w 8.2 aftershock is similar to the European results. Short-period observations from Japan show a bilateral rupture with most of the energy release concentrated to the NE and weak energy release to the SW. The rupture images from the F-net array are not as reliable as the European array images because of the apparent “swimming” artifacts that look as if energy is systematic drifting

in time in the direction towards Japan. The European results are not as conducive to the "swimming" artifact because the aperture of the array is larger.

3.3 P-waves from the Hi-Net Array in Japan

We improve upon the short-period results from Japan by using the Hi-net array. The Hi-net array is denser and has higher sensitivity than the F-net array. There are over 700 Hi-net stations (100 sps sampling rate) installed at depths of over 100 m in the bottom of boreholes. We used 766 vertical component recordings for the mainshock and 767 for the aftershock (Figure 10).

The most immediate difference between the Hi-net and F-net results is that bilateral rupture on the main fault plane is clearly present from Hi-net (see Figure 11 and 12). Aside from the initial rupture stage, the rest of the rupture is similar to F-net results. The rupture on a perpendicular fault as seen in the European results is more ambiguous from the observations in Japan. However, the energy release in the last rupture stage is more coherent than the F-net and European results.

The short-period observations of the large aftershock seem to be the most coherent in the Hi-net results (see Figure 13). Consistent with previous results, the initial rupture to the NE is followed by immediate rupture to the SW. The Hi-net images show the strongest evidence of rupture propagation to the SW. A clear subevent is imaged around 45 s with weaker radiation lasting to 80 s into the rupture.

Even though the F-net array aperture is larger than the Hi-net array, introducing a much denser observation of P-waves (about a factor of 10) helped to improve the resolution in imaging the short-period energy release from Japan and suppressed some amount of “swimming” artifacts. The bilateral rupture process is seen clearly in the mainshock and large aftershock.

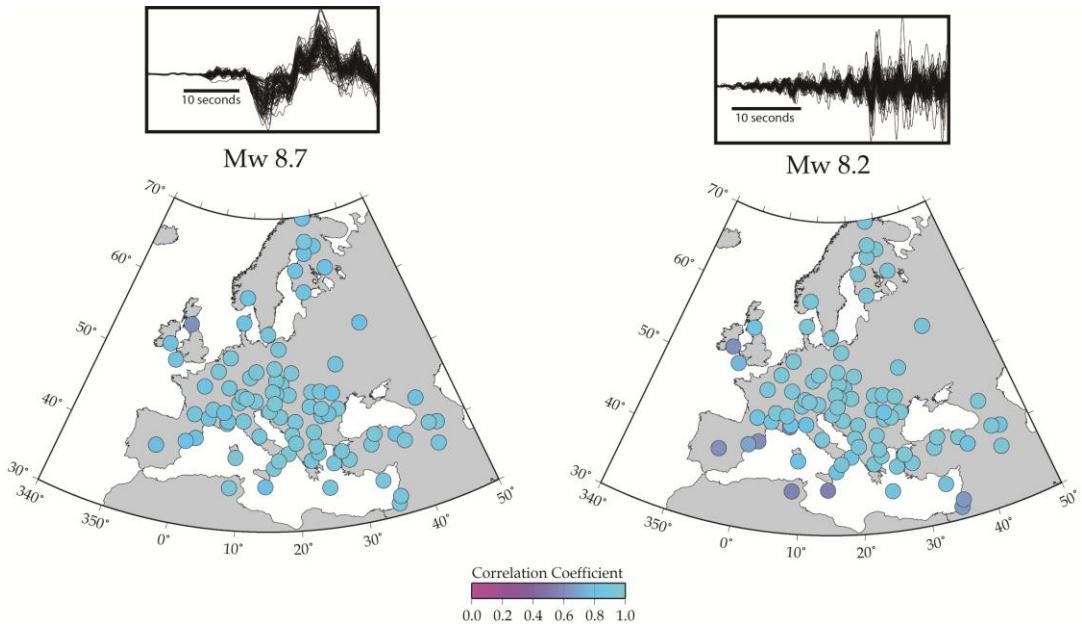

Figure 2. Aligned teleseismic waveforms and locations of seismograph stations in Europe that were used in the back-projection of the M_w 8.7 and M_w 8.2 Sumatra earthquakes. The cross-correlation coefficient for each station is indicated by the color scale.

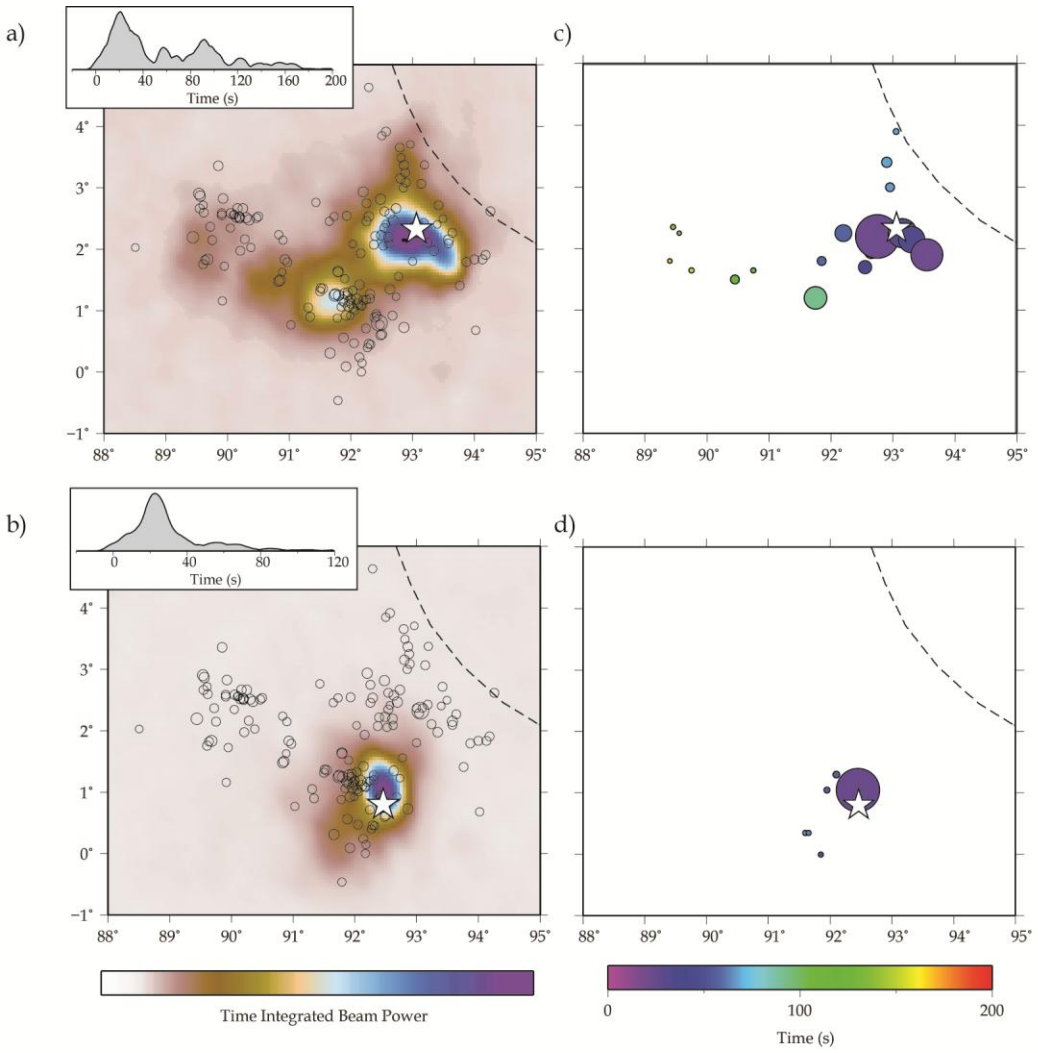

Figure 3. European array results of the time integrated beam power image for (a) the M_w 8.7 mainshock and (b) the M_w 8.2 aftershock. Beam power image ranging from zero (white) to unity (purple). Open circles are the first day of aftershock locations. Dashed lines outline the plate-boundary setting. Inset graphs show beam power amplitude as a function of time. Local maximum beam power plot for (c) the M_w 8.7 mainshock and (d) the M_w 8.2 aftershock. Color indicating lapse time from the origin time and circle size is proportional to beam power. White star indicates epicentral location.

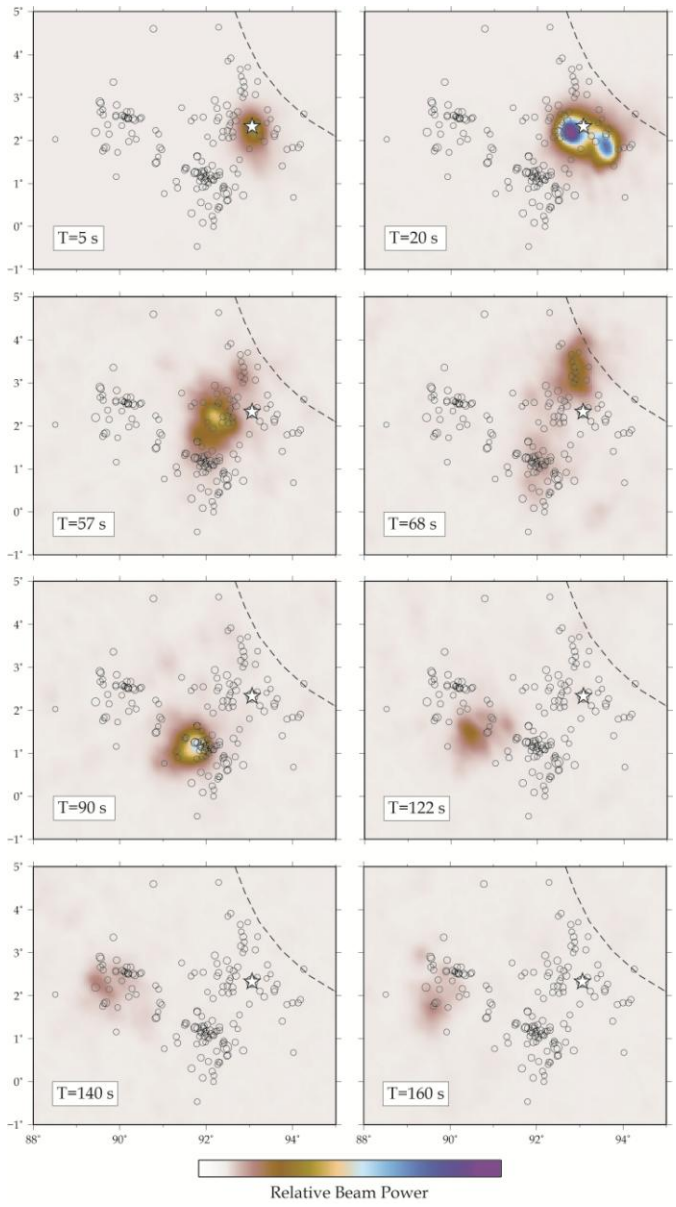

Figure 4. Snapshots of the M_w 8.7 rupture as imaged from the European array.

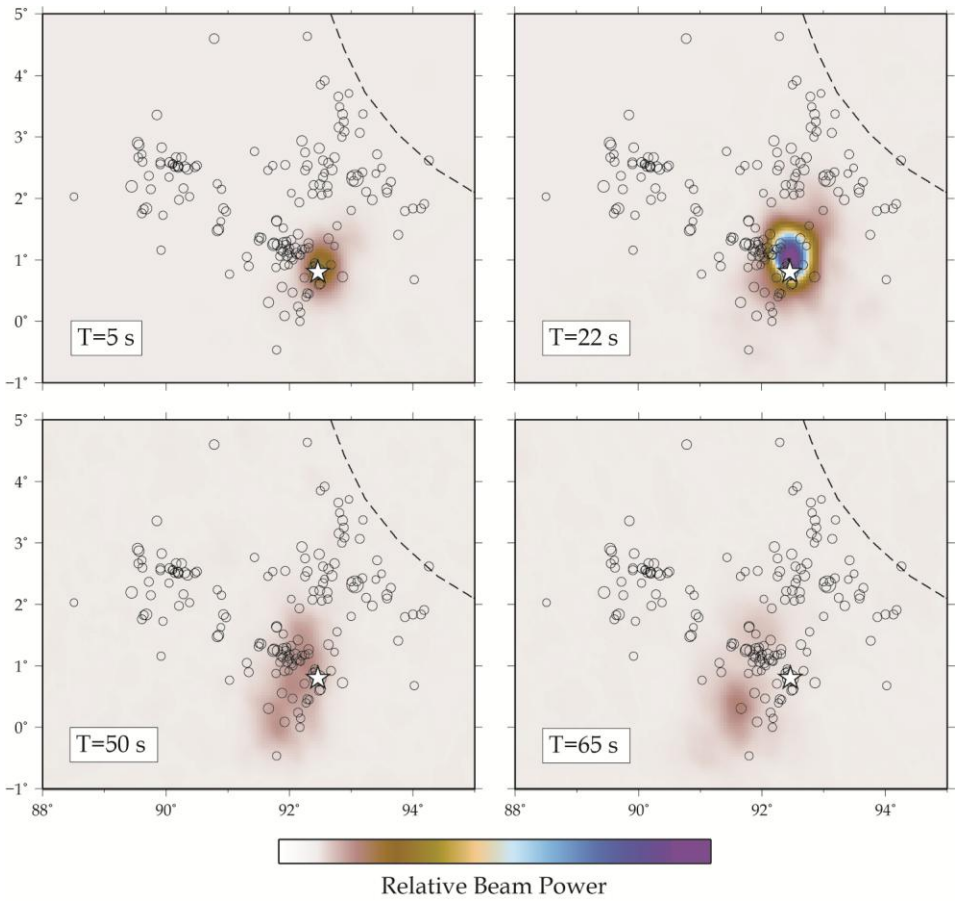

Figure 5. Snapshots of the M_w 8.2 rupture as imaged from the European array.

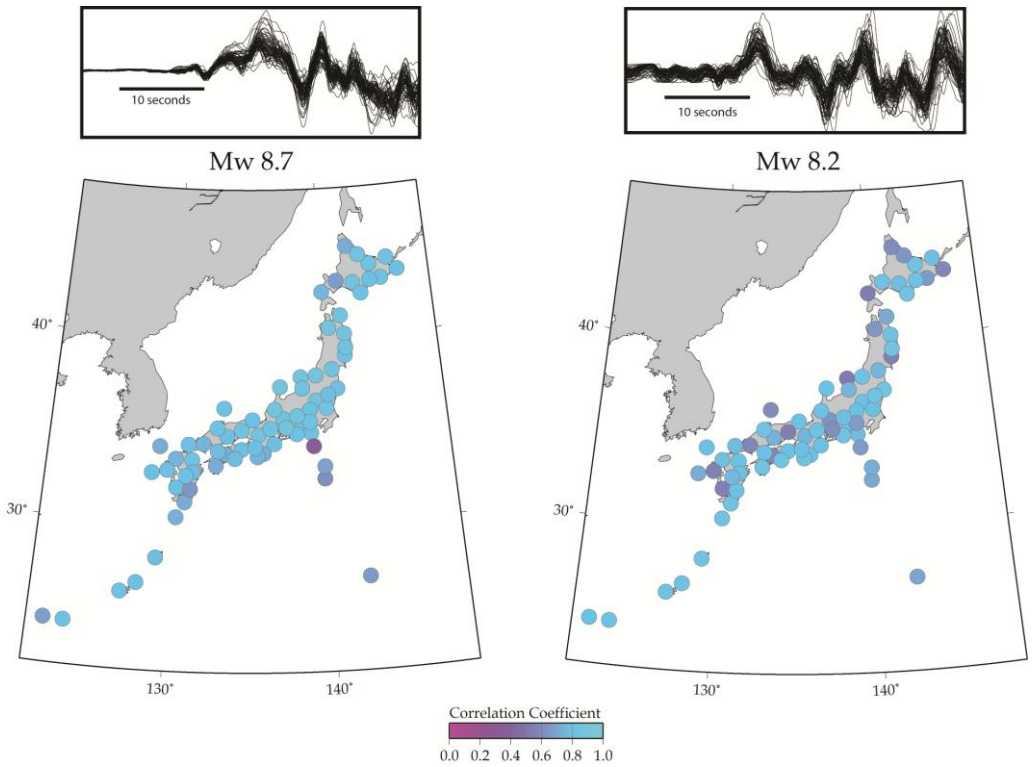

Figure 6. Aligned teleseismic waveforms and locations of seismograph stations of the F-net array in Japan that were used in the back-projection of the M_w 8.7 and M_w 8.2 Sumatra earthquakes. The cross-correlation coefficient for each station is indicated by the color scale.

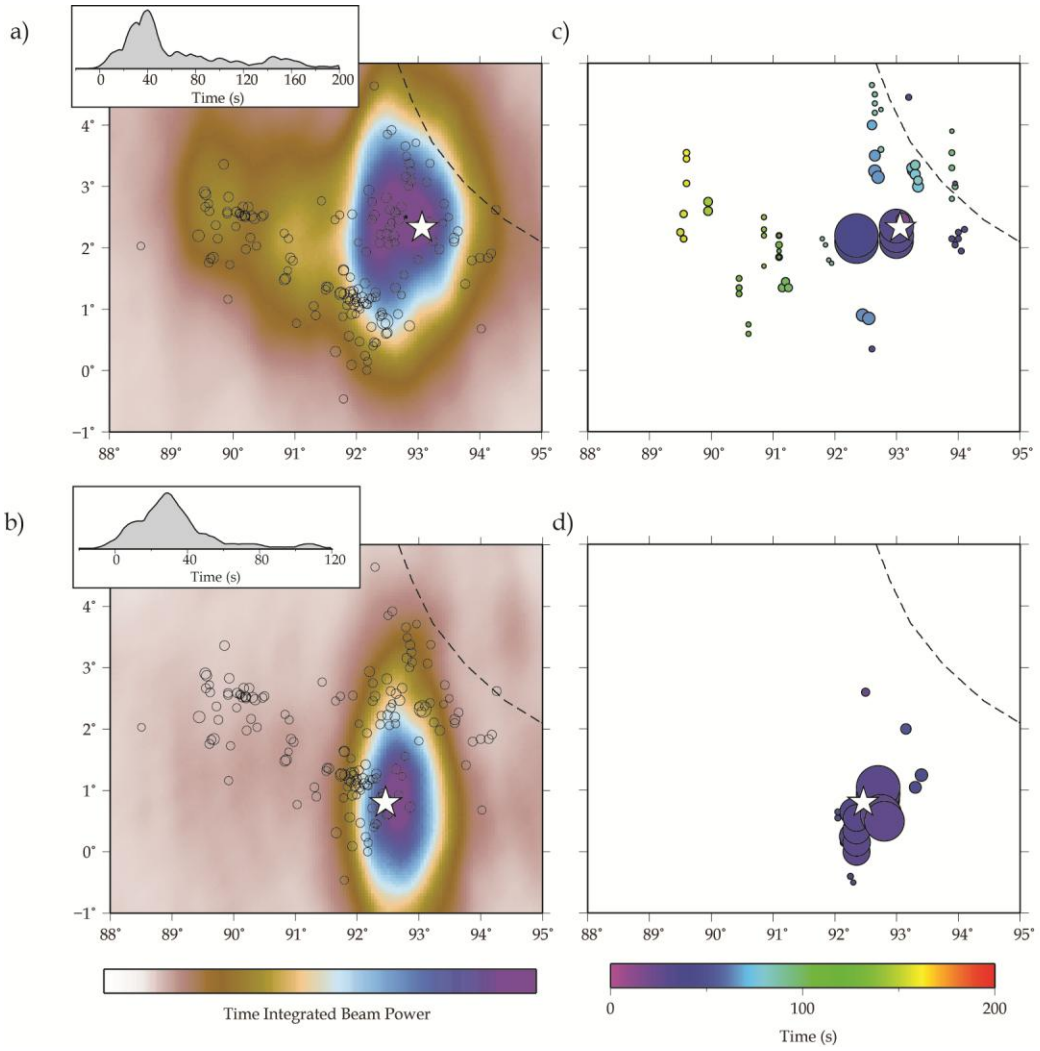

Figure 7. F-net array results of the time integrated beam power image for (a) the M_w 8.7 mainshock and (b) the M_w 8.2 aftershock. Beam power image ranging from zero (white) to unity (purple). Open circles are the first day of aftershock locations. Dashed lines outline the plate-boundary setting. Inset graphs show beam power amplitude as a function of time. Local maximum beam power plot for (c) the M_w 8.7 mainshock and (d) the M_w 8.2 aftershock. Color indicating lapse time from the origin time and circle size is proportional to beam power. White star indicates epicentral location.

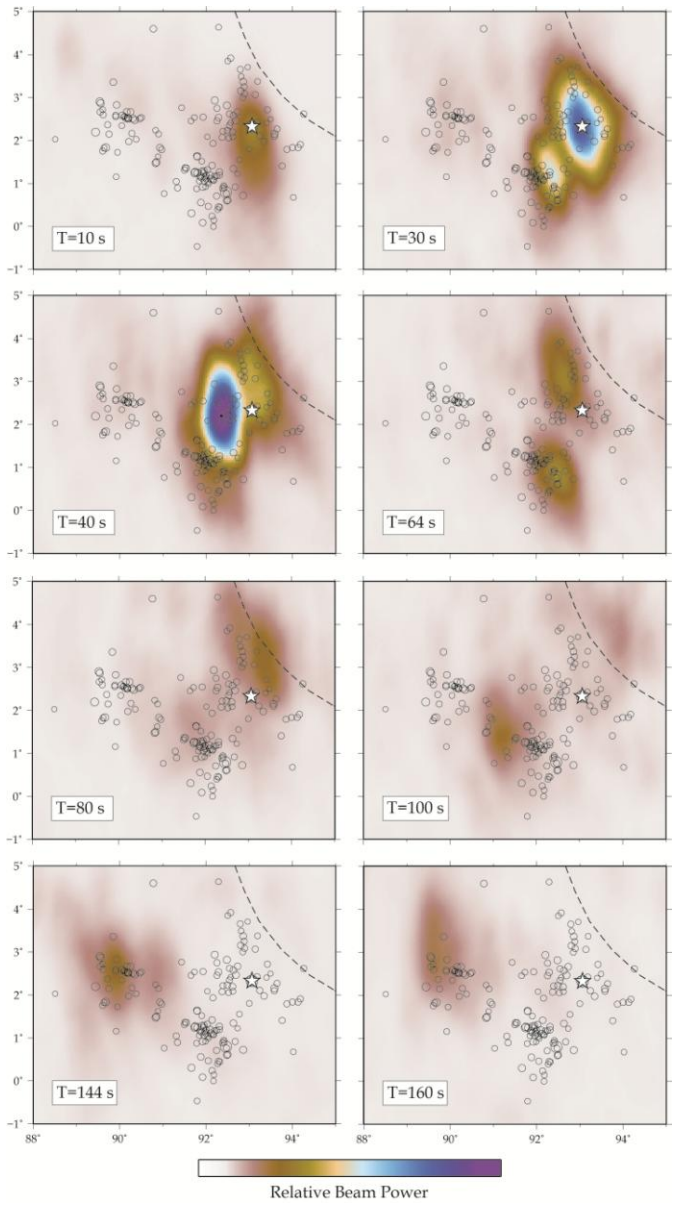

Figure 8. Snapshots of the M_w 8.7 rupture as imaged from the F-net array.

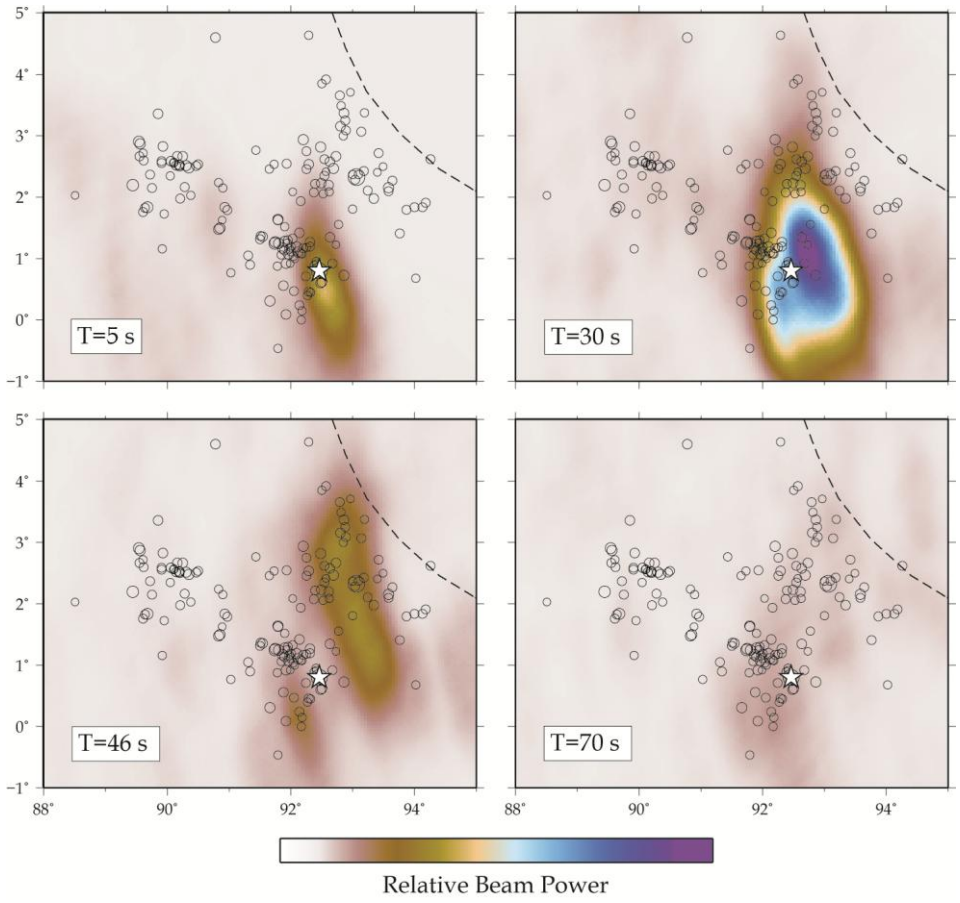

Figure 9. Snapshots of the M_w 8.2 rupture as imaged from the F-net array.

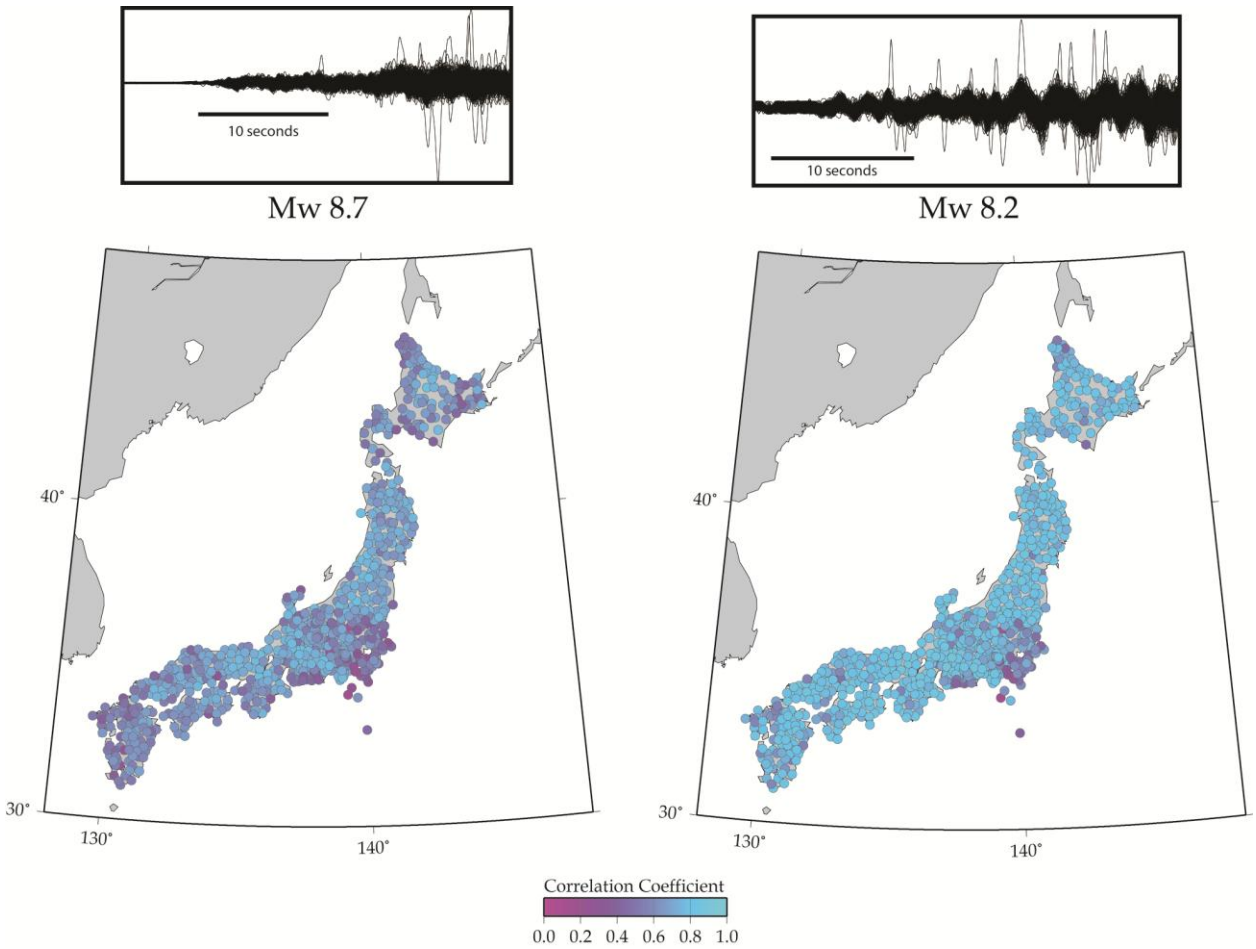

Figure 10. Aligned teleseismic waveforms and locations of seismograph stations of the Hi-net array in Japan that were used in the back-projection of the M_w 8.7 and M_w 8.2 Sumatra earthquakes. The cross-correlation coefficient for each station is indicated by the color scale.

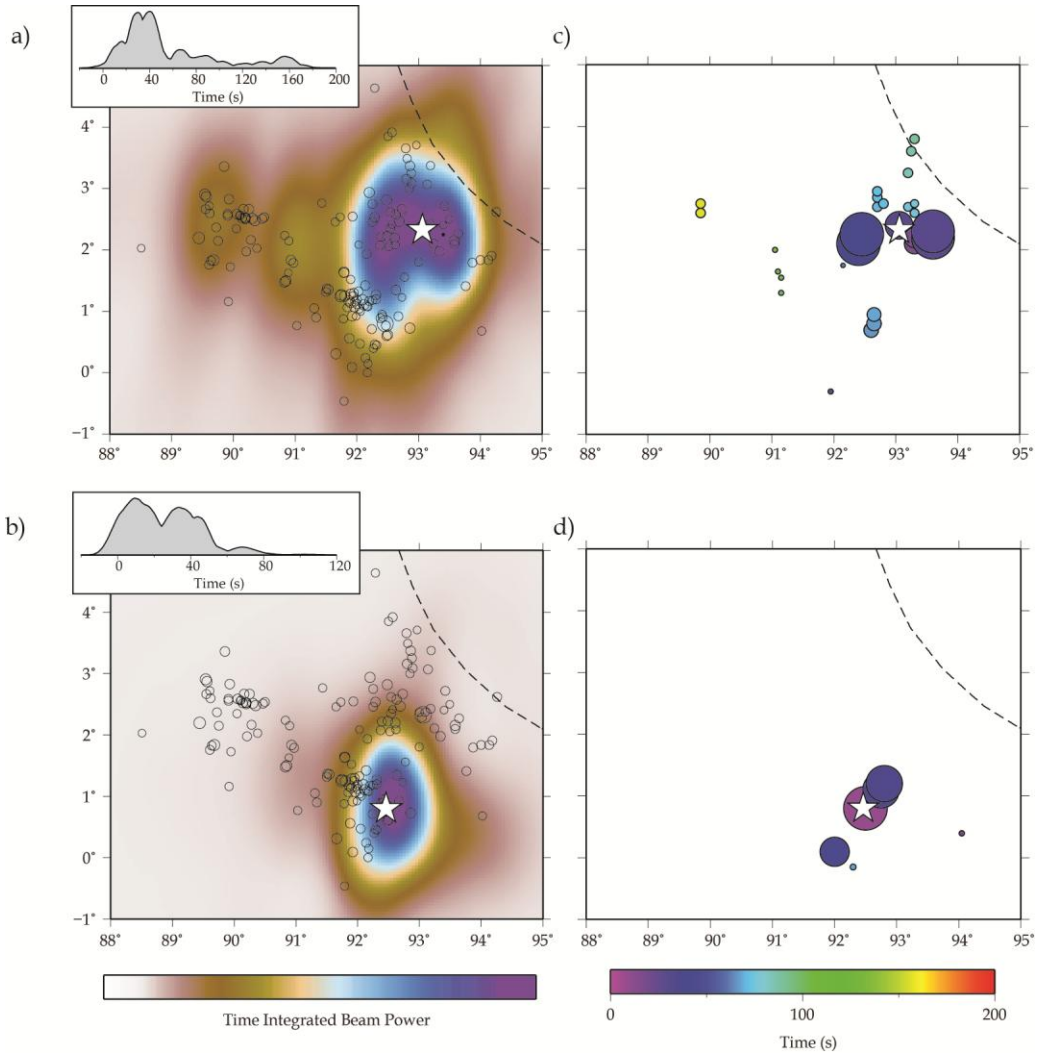

Figure 11. Hi-net array results of the time integrated beam power image for (a) the M_w 8.7 mainshock and (b) the M_w 8.2 aftershock. Beam power image ranging from zero (white) to unity (purple). Open circles are the first day of aftershock locations. Dashed lines outline the plate-boundary setting. Inset graphs show beam power amplitude as a function of time. Local maximum beam power plot for (c) the M_w 8.7 mainshock and (d) the M_w 8.2 aftershock. Color indicating lapse time from the origin time and circle size is proportional to beam power. White star indicates epicentral location.

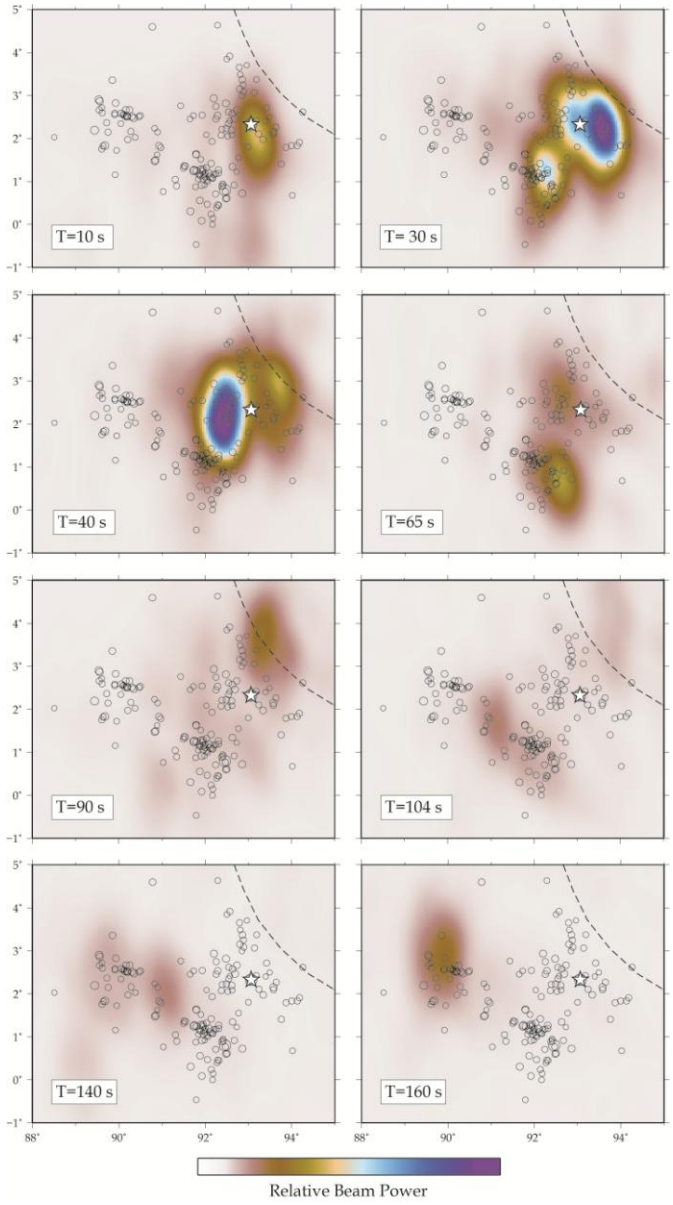

Figure 12. Snapshots of the M_w 8.7 rupture as imaged from the Hi-net array.

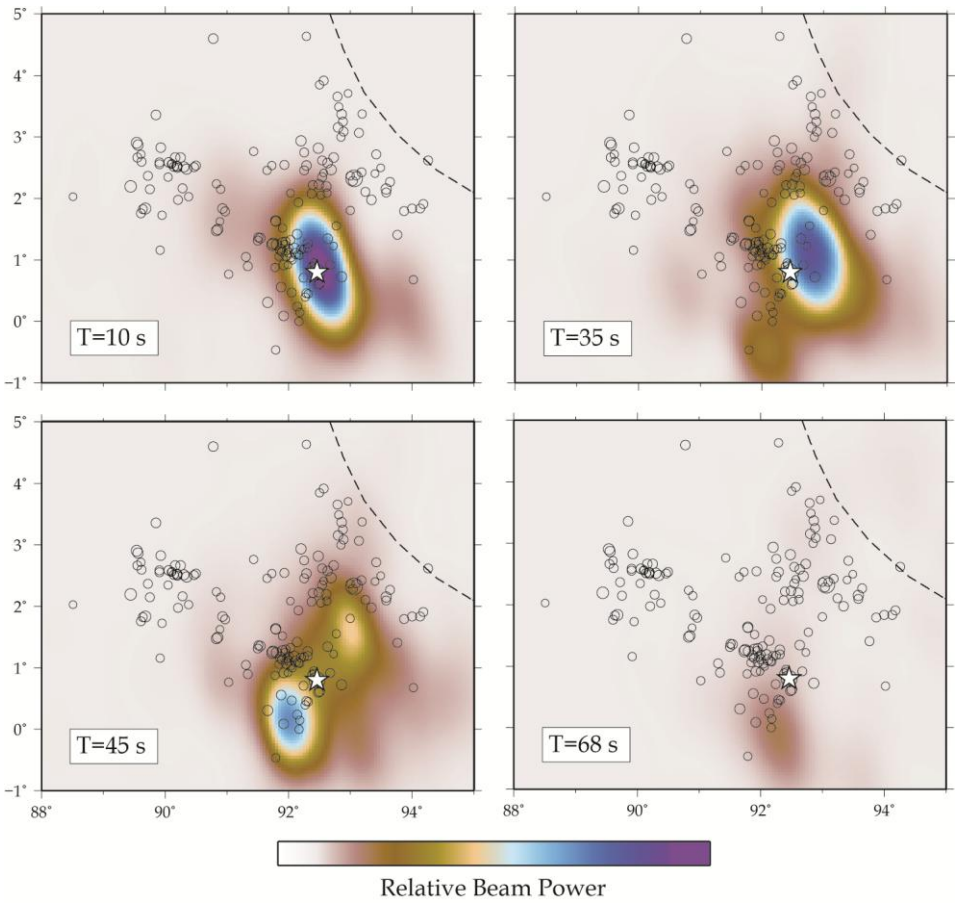

Figure 13. Snapshots of the M_w 8.2 rupture as imaged from the Hi-net array.

CHAPTER 4

SUBEVENT LOCATIONS

4.1 Exploring Mainshock Rupture Complexity

We have shown from the back-projection of P-waves that the M_w 8.7 mainshock ruptured on multiple faults over a wide area. The back-projection from the European array provides the most robust images of the short-period rupture showing multiple distinct subevent arrivals. Tracking the subevent locations helps to delineate the number and orientation of the faults for which the mainshock ruptured. The wide and intricate rupture extent suggests sensitivity to travel time anomalies due to wavefront distortion travelling in the real three-dimensional Earth structure. Our conventional approach is to apply a static travel time correction value to each grid point by cross-correlations of the P-waves and by using the estimation of the travel time for the path from the mainshock hypocenter to a seismometer. This approach might work well assuming that the whole rupture is near the hypocenter location. For this event, however, we propose a further set of empirical travel time corrections calculated at distances away from the hypocenter location.

4.2 Aftershock Time Correction

The 2004 M_w 9.1 Sumatra-Andaman earthquake ruptured unilaterally along the Sunda trench. The extent of that rupture is unprecedentedly long at about 1300 km, expanding from northern Sumatra to the Andaman Islands. Later in 2005, the M_w 8.6 Sumatra (Nias) earthquake occurred southeast near the 2004 epicenter but was found to have a compact bilateral rupture. To determine the rupture properties of these two Sumatran earthquakes, Ishii *et al*. [2007] corrected for the heterogeneity of the wave paths for grid points at larger distances to the 2004 and 2005 hypocenter location. To determine the corrections, they introduced a method that uses aftershocks to enhance the empirical set of travel time corrections applied over the whole grid region. Correction values were obtained by cross-correlating P-waves of large aftershocks occurring throughout the source region in order to generate a new set of static travel time corrections to be interpolated over the grid region. Therefore, each grid point has a different travel time correction value.

The idea of using aftershocks relates to the well-known observation that aftershocks occur in and around the rupture region on the mainshock fault plane. The inclusion of aftershocks attempts to provide a better constraint to estimate the travel time correction for a broad source region than the conventional method that uses only the mainshock hypocenter to seismometer travel time correction estimate. The study of Ishii *et al*. [2007] compared back-projection results of their aftershock time calibrated method to their hypocentral time estimate method for the giant 2004 and 2005 Sumatran events. They observed small-scale features of the rupture that are different between the two time correction methods. While the short-period source time function remains similar, the spatial distribution of the energy release shows some changes. Using more empirical

travel time corrections provides a better estimate of the subevent locations that are further away from the hypocenter location.

4.3 Calibrating the 2012 Indian Ocean Aftershocks

Inspired by the aftershock time correction method from Ishii *et al.* [2007], we replicate a similar procedure for the 2012 M_w 8.7 Indian Ocean mainshock. Our motivation is to use this new time correction method to observe potential changes in the spatial distribution of the short-period energy release. We applied cross-correlations of aftershock P-waves using the same set of European stations from the mainshock back-projection. We cross-correlated only aftershocks that were M_w 5.5 or larger as we expect better alignment of the P-waves pertaining to events of that size.

Aftershocks occurring near the time of the mainshock were harder to align due to the contamination from the mainshock signal. Including the M_w 8.2 aftershock, we were able to derive time shift correction values from seven aftershocks (see Figure 14). The number of aftershocks is sparse but their hypocenters are dispersed throughout the mainshock rupture area. As expected, the back-projections of the individual aftershocks all indicate compact point source like ruptures. The coherent back-projections validate the robustness of the time shift correction values. Including the mainshock, the eight static time shift values for each station are linearly interpolated to retrieve a value at each grid point. The time shift Δt_{ik} is calculated for each grid point *i* at station *k*

$$\Delta t_{ik} = (\sum_{j=1}^{m} \frac{w_j^n \Delta t_{jk}}{\Delta_{ij}}) / (\sum_{j=1}^{m} \frac{w_j^n}{\Delta_{ij}})$$

such that Δt_{jk} represents the time shift value of j^{th} aftershock from the k^{th} station. The time shift values are weighted where w_j^n represents the aftershock weighted value

according to the distance of the aftershocks to the grid point. The aftershocks that are closer to the grid point are given higher weights. The weighted values are raised to the *n* power of 1, 1.5 and 2. The summation of the time shift values is taken over *m* aftershocks.

4.4 Back-projection Images from New Time Corrections

We present new back-projection results of the mainshock by using the same procedure described in our methods section except we stacked our seismograms using the new travel time interpolated grid. The same set of European stations used in our preliminary results that applied only the hypocentral time shift correction is also used for the new aftershock time interpolated result. To compare our results, we show the time integrated (Figure 15) and local maximum (Figure 16) beam power images to illustrate the spatial variations of the short-period energy release. We applied three different power values (n=1,1.5,2) to our weights to explore the spatial time-shift variations of our grid, but the result of the time-integrated beam images looks identical from one another. However, we see some spatial variations in the local maximum beam power results.

The most striking observation is the spatial variations of the short-period energy release from our new aftershock time corrected versus the hypocentral time corrected image. The rupture propagation and the timing of the energy release between subevents appear to be similar, but small-scale changes of the locations of the subevents are evident. For example, the subevents appear to line up more linearly as shown (Figure 16) for the aftershock time correction as compared to the hypocentral time correction. As a result, linear fault plane trends seem to emerge when using the new corrections. Overall, we see

two parallel NNW trending planes and an orthogonal cross cutting plane. The last rupture stage might be connected to the second subparallel plane, but is separated in space and time and could be on a separate fault plane. We also show rupture images of our new back-projection result that show the same time frame images as Figure 4 except the last frame. The rupture in space and time are similar, but the biggest difference is in the last segment of the rupture. At 168 s, a coherent arrival previously unseen is now evident.

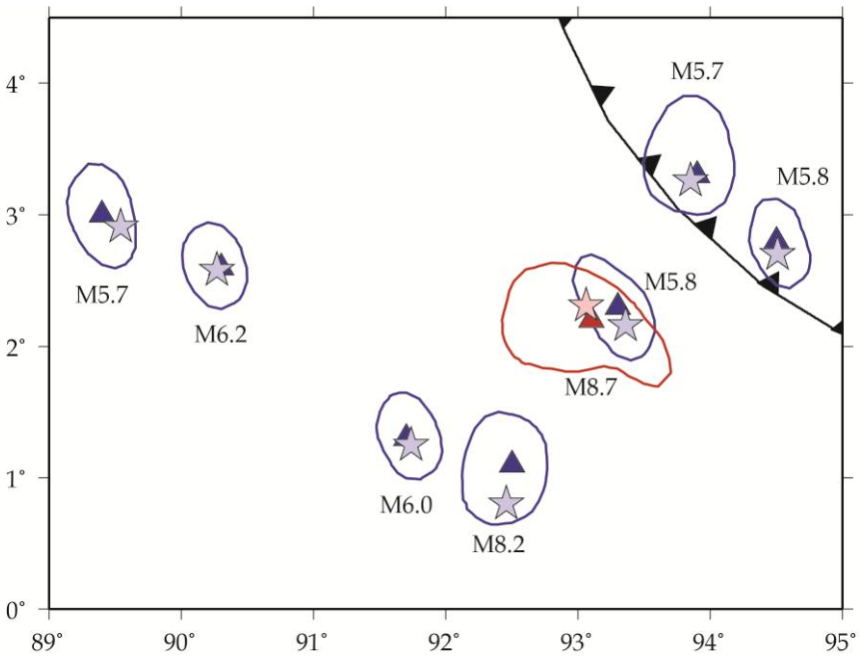

Figure 14. Events used in the interpolation of the travel-time correction for each grid point. The red star is the mainshock hypocenter location. Blue stars are aftershock hypocenters. The contours indicate the outline of the back-projection beam. The triangles indicate the location of peak energy release.

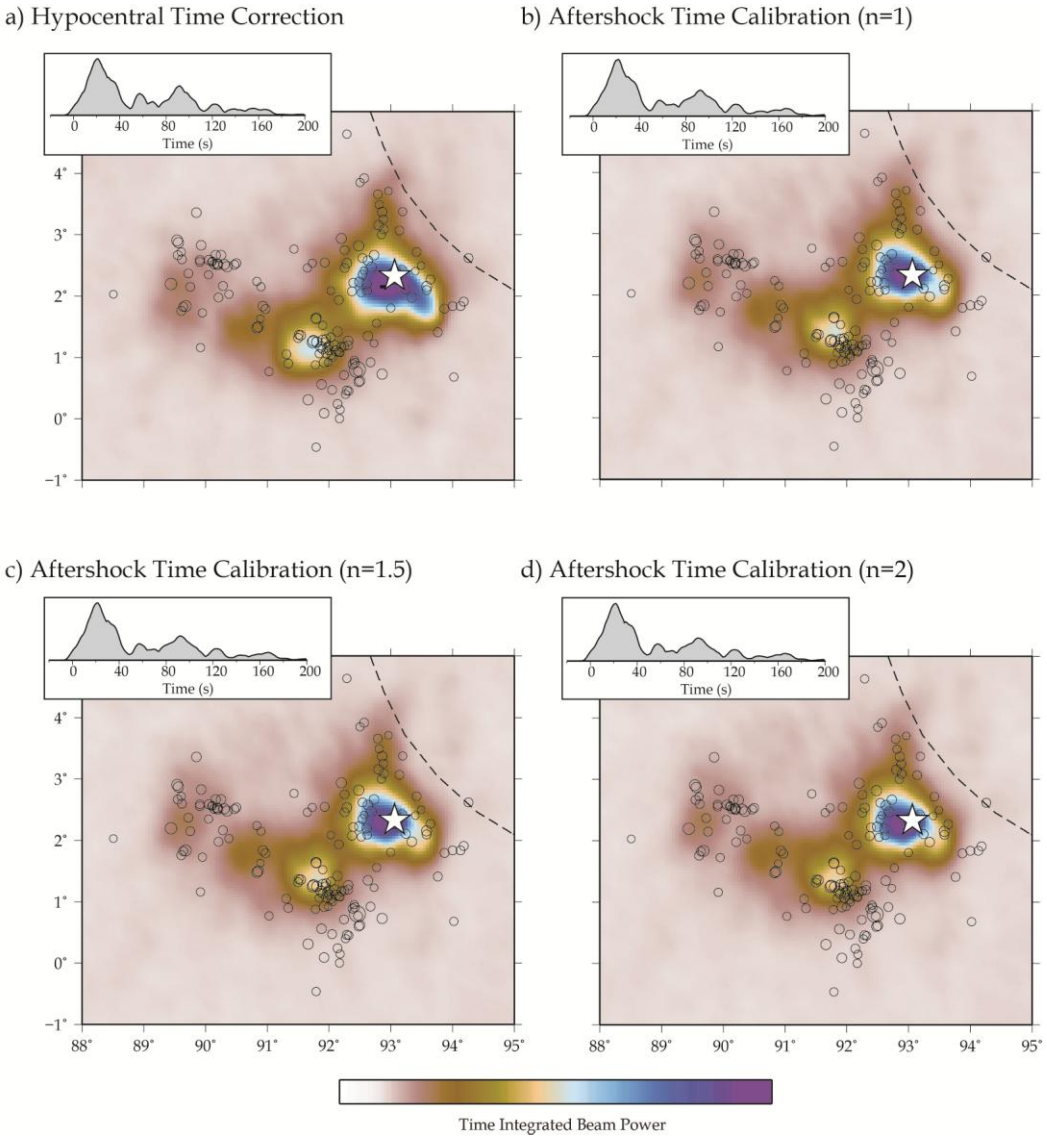

Figure 15. Time-integrated beam power image for the mainshock. Our conventional method uses (a) travel time corrections from the hypocenter to seismometer. The improved method interpolates travel time correction values of the mainshock and aftershocks for each grid point where the time correction is weighted by the distance of the grid point to each aftershock. The weights are raised to the powers of (b) 1, (c) 1.5, and (d) 2.

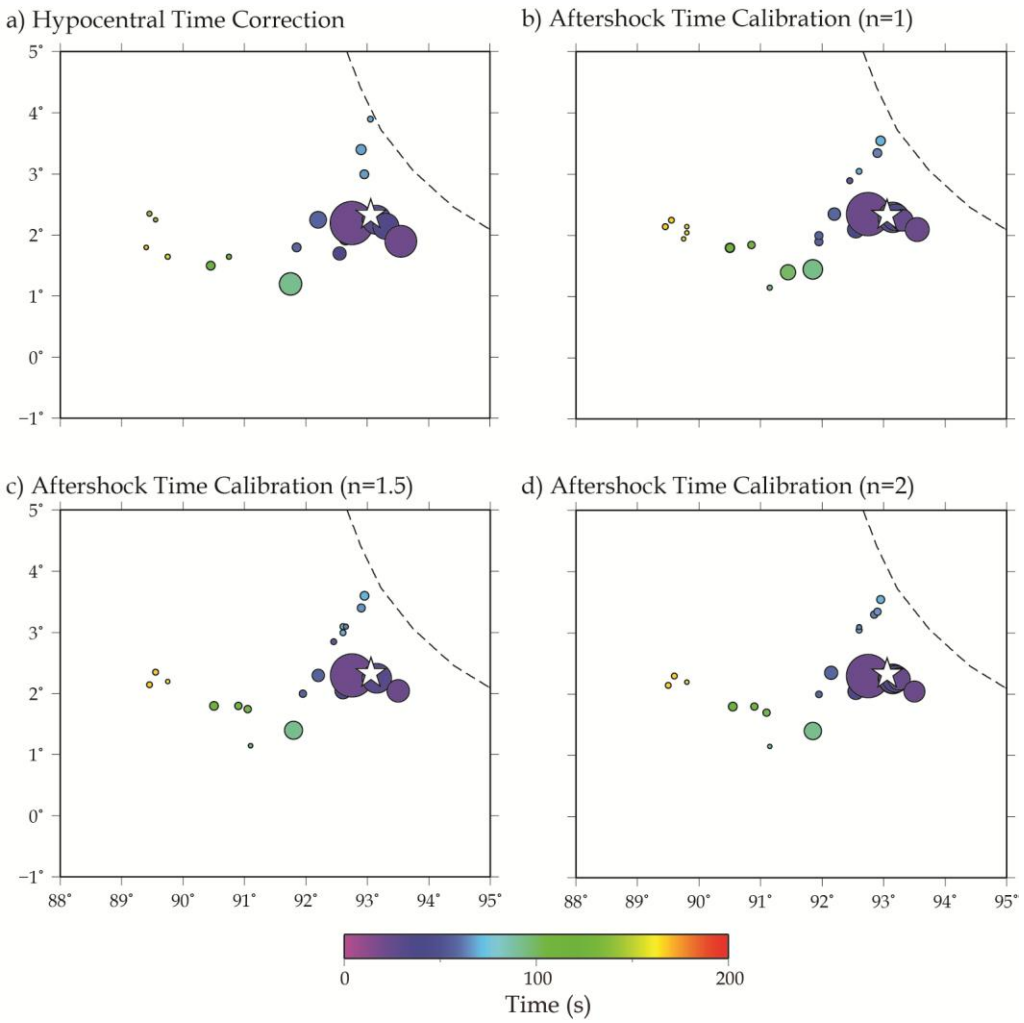

Figure 16. Similar description as Figure 15 but for the local maximum beam power amplitudes with respect to space and time.

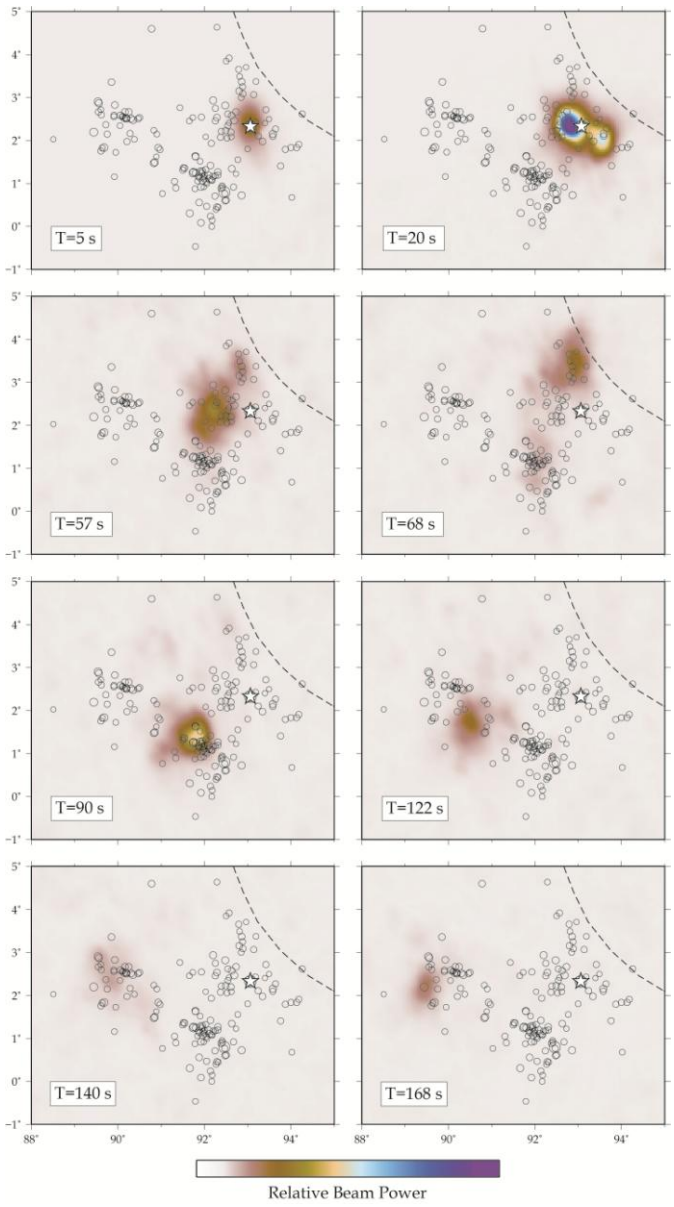

Figure 17. Snapshots of the M_w 8.7 rupture as imaged from the European array using aftershock interpolated travel time corrections.

CHAPTER 5

RECONCILING SOURCE MODELS

5.1 Back-Projection versus Finite Fault Models

The short-period rupture constraints from back-projection imaging have thus far provided the most detailed information about the space-time history of the mainshock rupture. Even though back-projection images from different groups have been consistent, interpretations of the faults that ruptured have varied. For instance, Satriano *et al*. [2012] preferred a complex westward propagating rupture that triggered on different N-S trending strike-slip faults. However, Yue *et al*. [2012] and Meng *et al*. [2012] prefer a conjugate fault system which includes rupture initiating on a WNW-ESE trending fault which later triggers onto a orthogonal secondary fault. Zhang *et al*. [2012] propose a similar geometry but prefer the secondary fault to be trending NNE-SSW and not orthogonal to the primary fault. The preference for faults orienting roughly North-South suggests reactivation of left-lateral motion on North-South trending paleo-transform faults in the region. For the June 18, 2000 (M_w 7.8) Wharton Basin earthquake, Robinson *et al*. [2001] performed broadband body wave analysis that showed two strike-slip sub-events ruptured simultaneously on two near-conjugate rupture planes. They concluded that the first subevent ruptured on an N-S trending paleo-transform fault and the second subevent ruptured on a 75° E-W trending fault plane. Abercrombie *et al*. [2003] modeled

similar results for the first strike-slip subevent, and in contrast to Robinson *et al*. [2001], preferred the second subevent to have reverse slip on the subduction interface.

The overall rupture speed determined by Meng *et al*. [2012] is ~2.5 km/s. Wang *et al*. [2012] found similar results, but only during the initial rupture stage. After 30 s from the origin time, Wang *et al*. [2012] propose that the rupture accelerates to 5 km/s and remains there until the final segment of the rupture at which time the rupture speed estimate becomes less reliable. The rupture speed of 5 km/s exceeds the local S-wave velocity which implies the involvement of supershear rupture. No other source model other than Wang *et al*. [2012] has proposed evidence of supershear rupture for this event.

The initial inversions of the mainshock fault model preferred slip on a single roughly N-S plane. The complex aftershock distribution and short-period back-projection images helped parameterize the inversion of multiple conjugate fault planes. However, Shao and Ji [2012] prefer the primary and secondary fault to be subparallel from one another and striking NNE-SSW, whereas Yue *et al*. [2012] prefer the primary and secondary fault to be orthogonal from one another. For the primary fault inversion, the data fit better to the synthetic waveforms for an N-S oriented plane than an E-W plane. Yue *et al*. [2012] argue that waveform fits improved for an E-W plane if the primary fault included two subfaults that are dipping in the opposite direction. A similar fault inversion result involving two oppositely dipping fault planes is proposed for the 1995 Kobe earthquake from Yoshida *et al*. [1996].

5.2 Synthetic Data from Slip Models

We obtained four finite fault slip models of the mainshock from Han Yue and Dr. Thorne Lay at the University of California, Santa Cruz (see Appendix). The parameterized slip models have three different fault geometries. Two models includes a primary fault trending WNW-ESE with one model involving a secondary conjugate fault trending NNE-SSW and the other model involving a secondary conjugate fault orthogonal to the primary fault. The third fault model geometry includes the primary and secondary fault occurring on subparallel faults trending NNE-SSW. The fourth fault model has conjugate fault geometry but is parameterized to allow rupture at 5 km/s.

Synthetic seismograms from an array can be calculated based on the parameterization of the slip model. We will evaluate the four slip models by back-projecting synthetic seismograms (e.g., *Koper et al.* 2012). The motivation is to compare the consistency between slip-model observations from teleseismic and regional, high-rate GPS data to our high-passed teleseismic observations from back-projection. Although back-projection images are more sensitive to slip-rate, we expect some level of correspondence to the slip-model. We present our back-projections of synthetic seismograms modeled after the same set of European stations used in the real data back-projections corresponding to each of the four computed slip models from Han Yue and Dr. Thorne Lay.

5.3 Synthetic Data Back-projection Results

Comparing the real data image to the synthetics, we see major differences between the beam power images (Figure 18). Expectedly though, all the models show short-period energy release within the aftershock zone. It is interesting to see that all the synthetic

models except for the supershear model do not show a bilateral rupture on the primary fault. However, the supershear model looks the least similar to the real data image. Stronger energy release is seen to occur at later portions of the rupture such that the last major subevent is located beneath the second last strongest subevent after a long north-westward propagating sequence (Figure 19).

The energy release for the subparallel fault model is oriented NNE-SSW which is expected, but does not resemble the image of the real data as well. For the conjugate fault model, the peak energy is located NNW of the hypocenter such that the whole beam image looks shifted from the real data locations. Although bilateral rupture on the primary fault does not show up in the orthogonal fault model, it resembles the real data image the most. At higher frequency, it appears that the synthetic results are not as sensitive to all the portions of slip on the fault. In fact, the discrepancy between the locations of short-period energy and slip might be larger than realized.

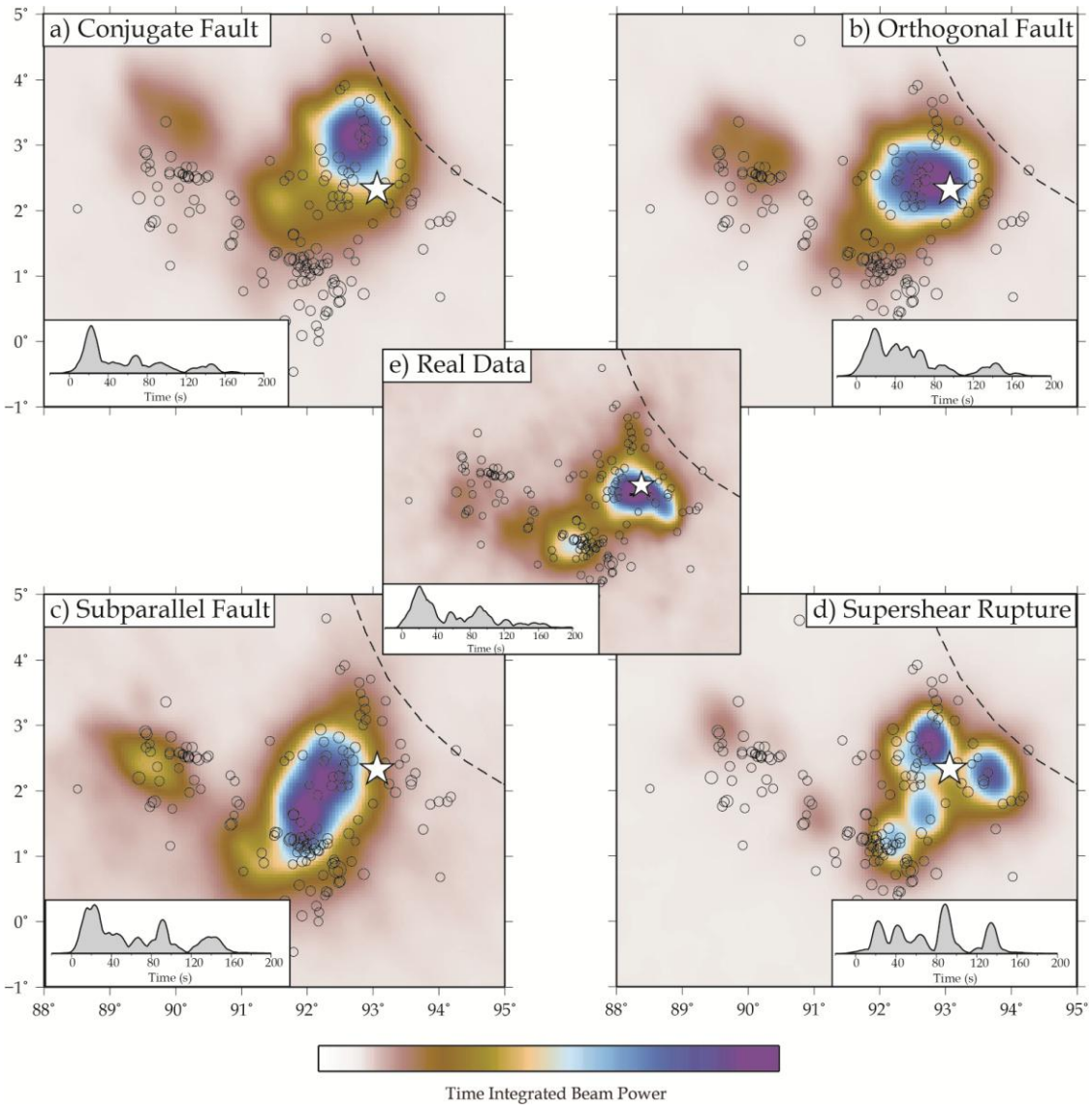

Figure 18. Time-integrated beam images of the back-projection of synthetic data from the European array and modeled from a (a) conjugate fault and an (b) orthogonal fault, a (c) subparallel and (d) supershear rupture slip model. The (e) real data back-projection is included in the middle for comparison.

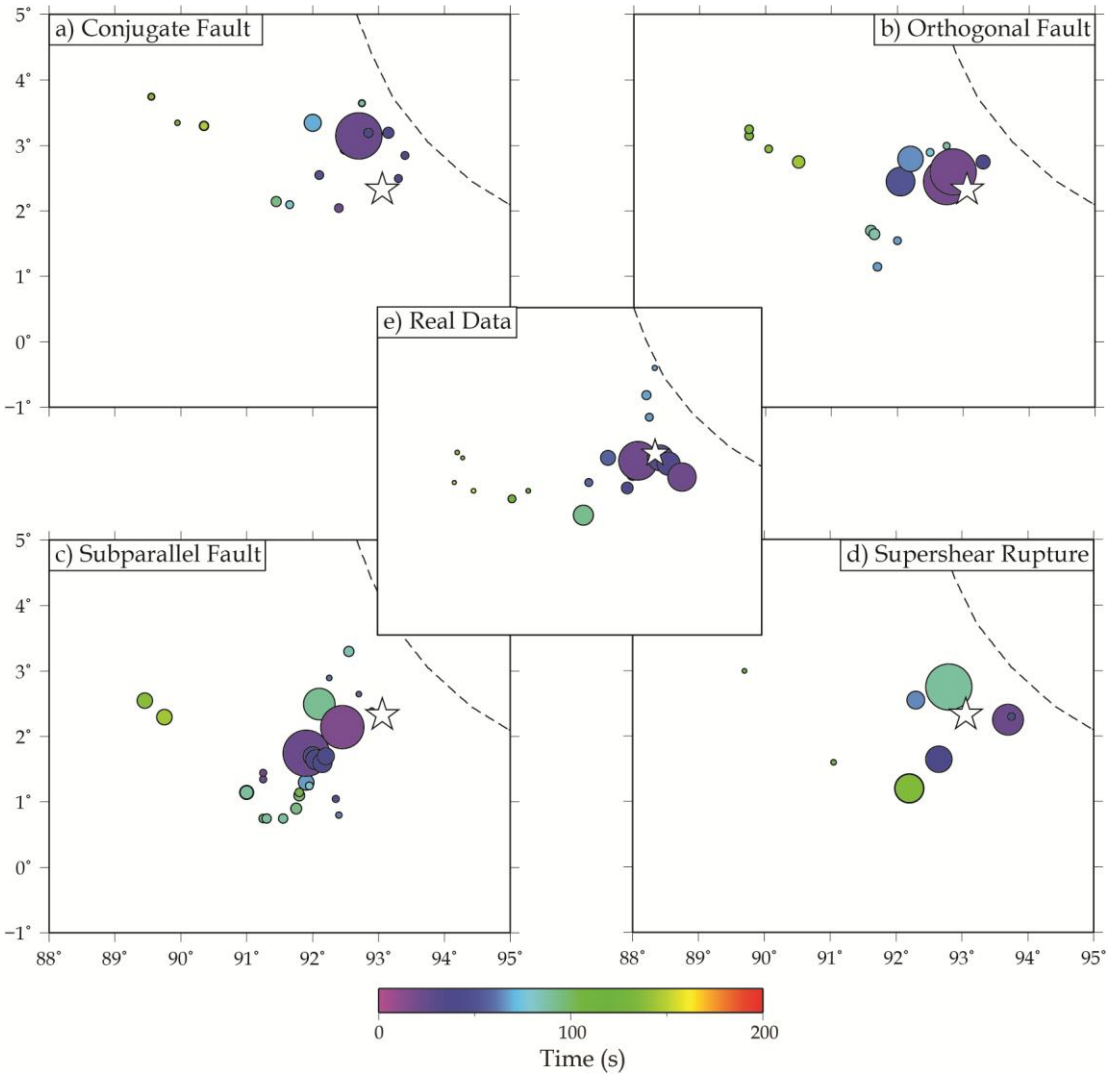

Figure 19. Similar description as Figure 18 but showing the local maximum beam power amplitudes with respect to space and time.

CHAPTER 6

DISCUSSION AND CONCLUSION

6.1 Summary of Results

An immediate validation of our back-projection results was that the locations of short-period energy coincided with the aftershock distribution. Our most robust back-projection images came from using 85 broadband stations in Europe. The aperture of the European array is larger than the F-net and Hi-net array in Japan and provided a better resolution of the beamed image.

We conclude that the mainshock ruptured on 4 main fault segments (Figure 20). The 1st rupture stage initiated on a WNW-ESE primary fault plane and later branched into a 2nd rupture stage on a orthogonal cross-cutting fault plane with respect to the west side of the primary fault. The 3rd rupture stage occurred on a fault plane parallel and south from the primary fault and propagated unilaterally westward. The 4th and last rupture stage occurred on an ambiguous fault plane around the western most part of the aftershock sequence.

Including aftershocks in estimating travel time corrections for each grid point improved our back-projection images. The new aftershock interpolated grid helps to compensate for the 3D variations in earth structure more so than using the hypocentral time correction. Enhanced linear features of the maximum beam power amplitudes in

space and time are presented in our improved back-projection images. The synthetic back-projections of an orthogonal fault model seemed to show the most similarity to the real data back-projections and thus further supported our preferred fault model.

Because there is no proposed finite fault solution for the M_w 8.2 event, back-projection imaging of the large aftershock has provided the most detailed analysis of the source. Our back-projection results showed bilateral short period energy release trending NNE-SSW with stronger energy emitting to the NNE (Figure 20). The rupture appeared to occur on a single fault plane and lasted about as half as long as the mainshock.

6.2 Significance of Results

Due to the fact that teleseismic data provided the most accessible observation of the 2012 Indian Ocean earthquake, back-projection imaging became the most robust method to track the space-time history of the rupture. Using back-projection to locate sources of short-period energy release over a wide grid space provides more freedom to search for potential activated faults without needing prior knowledge of the fault plane. Whereas in finite fault modeling, only the specific fault parameter assigned is inverted and thus not as helpful to rapidly locate unrealized subfaults.

The lack of regional seismic and geodetic observations together with the difficulty of direct geologic mapping of the rupture area has provided limited observations of the source region. The back-projection method clearly showed an advantage in probing the reactivation of paleo-transform faults and conjugate fault planes which has improved the finite fault modeling of the mainshock.

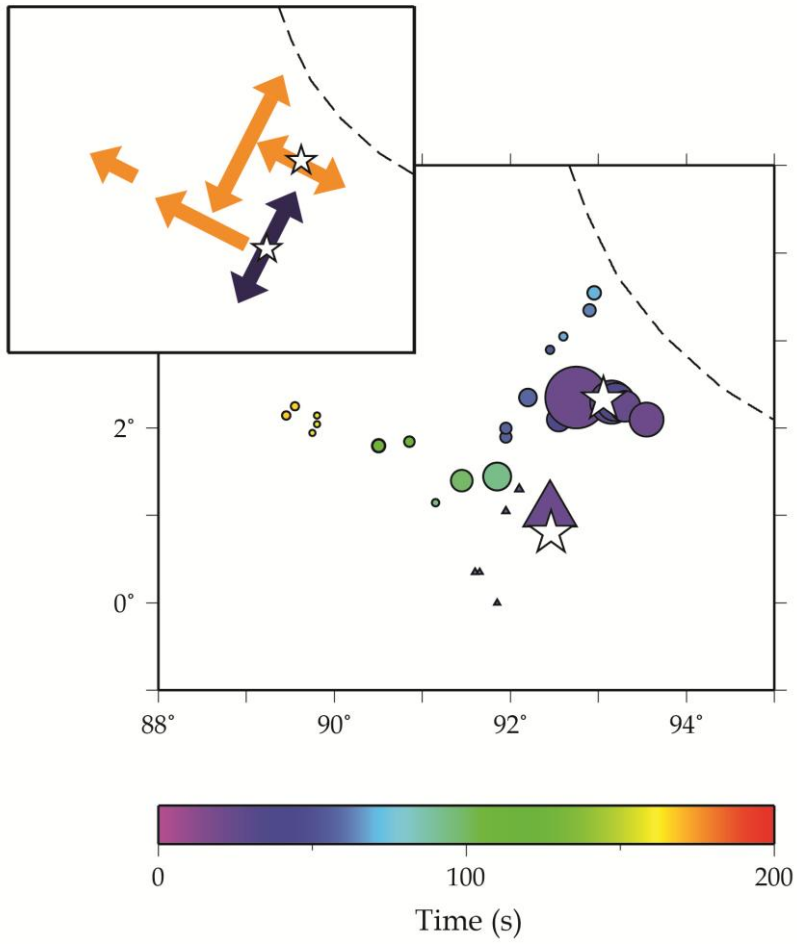

Figure 20. Summary of the European array back-projection results. Local maximum beam power locations for the M_w 8.7 mainshock (circles) and the M_w 8.2 aftershock (triangles). Color indicating lapse time from the origin time and shape size is proportional to beam power. Inset map illustrates the preferred rupture propagation along conjugate fault planes concluded in this study. The orange arrows represent rupture for the mainshock and the blue arrows represent rupture for the aftershock. Dashed lines represent plate boundary location and white stars represent epicentral locations of the mainshock and aftershock.

APPENDIX

SLIP MODELS

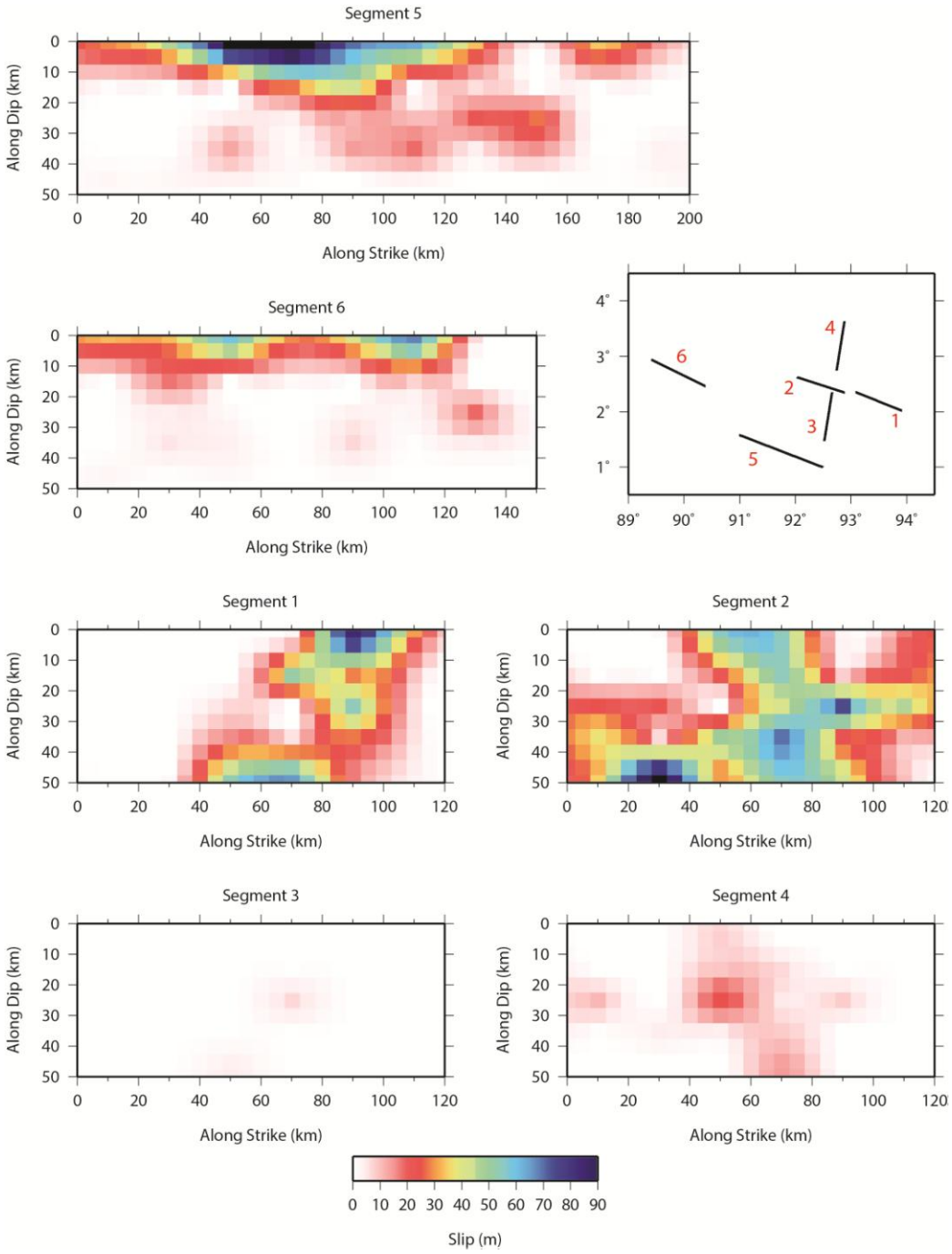

Figure 21. Conjugate fault slip model. Segment 3 and 4 are oriented NNE-SSW.

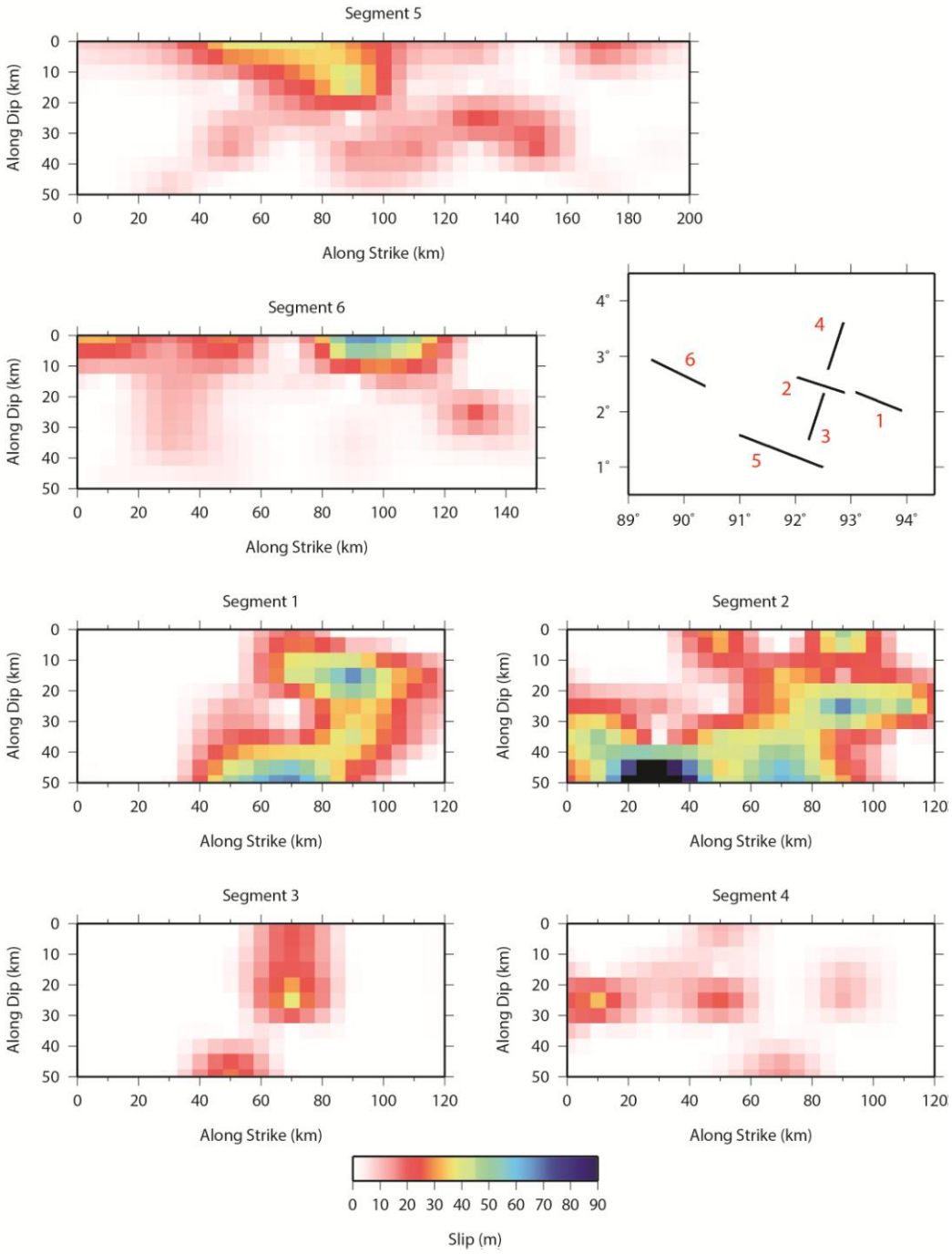

Figure 22. Orthogonal fault slip model. Segment 3 and 4 are orthogonal to the primary subfault segment 2.

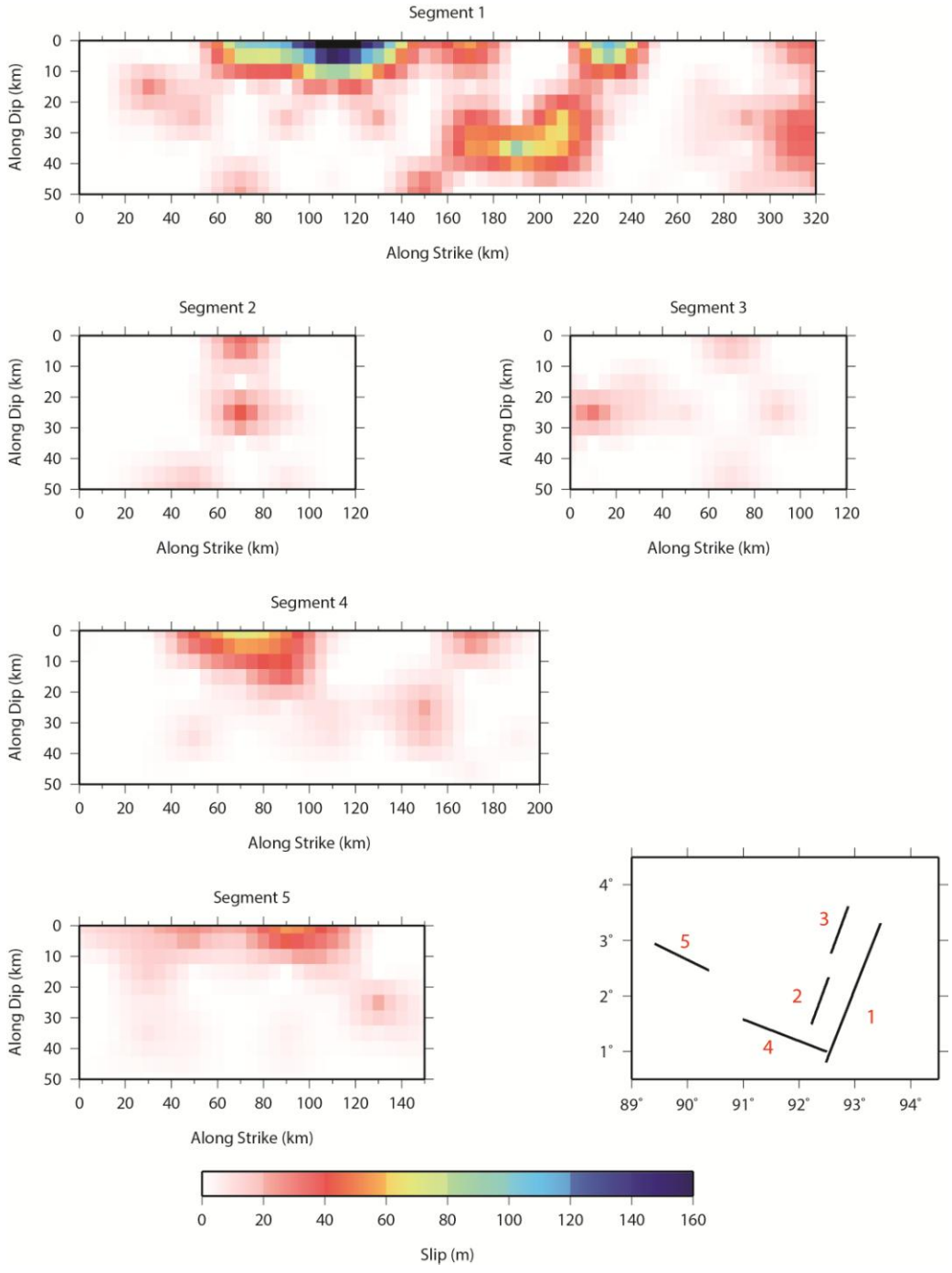

Figure 23. Subparallel fault model. Segments 2 and 3 are subparallel to segment 1.

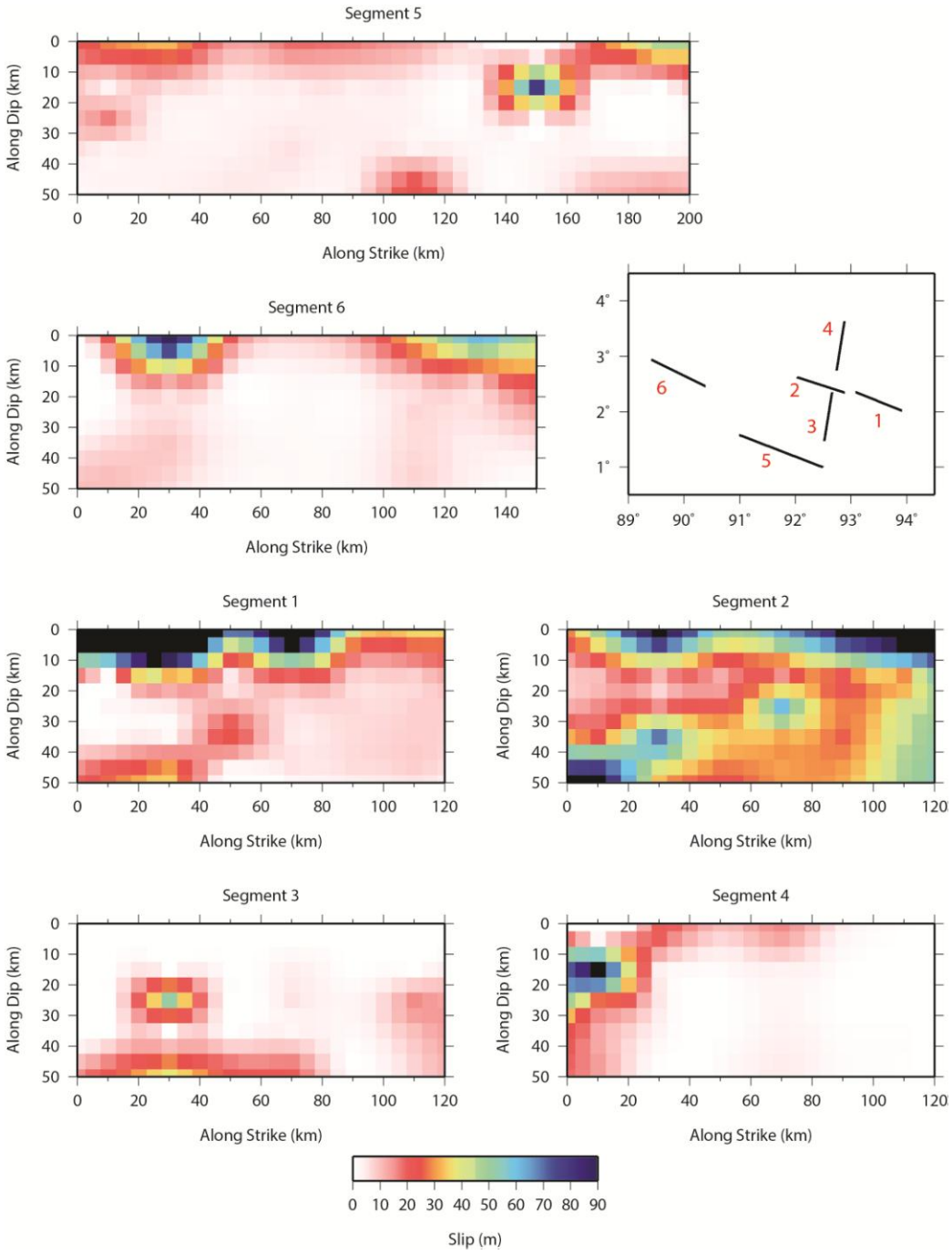

Figure 24. Super-shear rupture model. This model has the same geometry prescribed in the conjugate fault model but is parameterized to allow super-shear rupture to about 5 km/s.

REFERENCES

Abercrombie, R. E., M. Antolik, and G. Ekström (2003), The June 2000 Mw 7.9 earthquakes south of Sumatra: Deformation in the India-Australia Plate, *J. Geophys. Res.*, *108*(B1), 2018, doi:10.1029/2001JB000674.

Alex Hutko (2012), Back projections for Mw 8.7 off W coast of Northern Sumatra. http://www.iris.edu/spud/backprojection/118733.

Bergman, E. A., and S. C. Solomon (1984), Source mechanisms of earthquakes near mid-ocean ridges from body waveform inversion: Implications for the early evolution of oceanic lithosphere, *J. Geophys. Res.*, 89, 11,415-11,441.

Delescluse, M., and N. Chamot-Rooke (2007), Instantaneous deformation and kinematics of the India-Australia Plate, *Geophys. J. Int.*,168, 818–842, doi:10.1111/j.1365-246X.2006.03181.x.

Hayes, G. (2012), Preliminary Result of the Apr 11, 2012 Mw 8.6 Earthquake Off the West Coast of Northern Sumatra.
http://earthquake.usgs.gov/earthquakes/eqinthenews/2012/usc000905e/finite_fault.php.

Ishii, M., P. M. Shearer, H. Houston, and J. E. Vidale (2005), Extent, duration and speed of the 2004 Sumatra-Andaman earthquake imaged by the Hi-net array, *Nature*, 435, 933–936.

Ishii, M., P. M. Shearer, H. Houston, and J. E. Vidale (2007), Teleseismic P wave imaging of the 26 December 2004 Sumatra-Andaman and 28 March 2005 Sumatra earthquake ruptures using the Hi-net array, *J. Geophys. Res*., 112, B11307, doi:10.1029/2006JB004700.

Kennett, B. L. N., E. R. Engdahl, and R. Buland (1995), Constraints on seismic velocities in the Earth from travel times, *Geophys. J. Int.*, 122, 108–124, doi:10.1111/j.1365-246X.1995.tb03540.x.

Kiser, E., and M. Ishii (2012), Preliminary rupture modeling of the April 11, 2012 Sumatran earthquakes. http://www.seismology.harvard.edu/research_sumatra2012.html.

Koper, K. D., A. R. Hutko, T. Lay, and O. Sufri (2012), Imaging short-period seismic radiation from the 27 February 2010 Chile (M_W 8.8) earthquake by back-projection of *P*, *PP*, and *PKIKP* waves, *J. Geophys. Res.*, 117, B02308, doi:10.1029/2011JB008576.

Kruger, F., and M. Ohrnberger (2005), Spatio-temporal source characteristics of the 26 December 2004 Sumatra earthquake as imaged by teleseismic broadband arrays, *Geophys. Res. Lett.*, 32, L24312,doi:10.1029/2005GL023939.

McFadden, P. L., B. J. Drummond, and S. Kravis (1986), The Nth root stack: Theory, applications, and examples, *Geophysics*, 51, 1879–1892, doi:10.1190/1.1442045.

Meng, L., J.-P. Ampuero, J. Stock, Z. Duputel, Y. Luo, and V. C. Tsai (2012), Earthquake in a maze: compressional rupture branching during the 2012 MW 8.6 Sumatra earthquake, *Science*, 337, 724-726, doi:10.1126/science.1224030.

Robinson, D. P., C. Henry, S. Das, and J. H. Woodhouse (2001), Simultaneous rupture along two conjugate planes of the Wharton Basin earthquake, *Science*, 292, 1145–1148.

Royer, J.Y. and R.G. Gordon (1997), The Motion and Boundary Between the Capricorn and Australian Plates, *Science*, 277, 1268–1274.

Satriano, C., E. Kiraly, P. Bernard, and J.-P. Vilotte (2012), The 2012 M_w 8.6 Sumatra earthquake: Evidence of westward sequential seismic ruptures associated to the reactivation of a N-S ocean fabric, *Geophys. Res. Lett.*, 39, L15302, doi:10.1029/2012GL052387.

Shao, G. and C. Ji (2012), Spatiotemporal evolution of the 2012 Mw 8.6 Sumatra earthquake constrained by teleseismic body and surface waves, Abstract S31A-2486 presented at 2012 Fall Meeting, AGU, San Francisco, Calif., 3-7 Dec.

Shao, G., Li, X., C. Ji (2012), Preliminary Result of the Apr 11, 2012 Mw 8.64 sumatra Earthquake.
http://www.geol.ucsb.edu/faculty/ji/big_earthquakes/2012/04/10/sumatra.html.

Spudich, P., and E. Cranswick (1984), Direct observation of rupture propagation during the 1979 Imperial Valley, California, earthquake using a short-baseline accelerometer array, *Bull. Seismol. Soc. Am.*,74, 2083–2114.

VanDecar, J. C., and R. S. Crosson (1990), Determination of teleseismic relative phase arrival times using multi-channel cross-correlation and least squares, *Bull. Seismol. Soc. Am.*, 80, 150–169.

Wang, D., J. Mori, and T. Uchide (2012), Supershear rupture on multiple faults for the M_w 8.6 Off Northern Sumatra, Indonesia earthquake of April 11, 2012, *Geophys. Res. Lett.*, 39, L21307, doi:10.1029/2012GL053622.

Xu, Y., K. D. Koper, O. Sufri, L. Zhu, and A. R. Hutko (2009), Rupture imaging of the M_w 7.9 12 May 2008 Wenchuan earthquake from back projection of teleseismic P waves, *Geochem. Geophys. Geosyst.*, 10, Q04006, doi:10.1029/2008GC002335.

Yoshida, S., K. Koketsu, B. Shibazaki, T. Sagiya, T. Kato, and Y. Yoshida (1996), Joint inversion of the near- and far-field waveforms and geodetic data for the rupture process of the 1995 Kobe earthquake, *J. Phys. Earth*, 44,437–454.

Yue, H., T. Lay, and K. D. Koper (2012), En echelon and orthogonal fault ruptures of the 11 April 2012 great intraplate earthquakes, *Nature*, 490, 245–249, doi:10.1038/nature11492.

Zhang, H., J. Chen, and Z. Ge (2012), Multi-fault rupture and successive triggering during the 2012 Mw 8.6 Sumatra offshore earthquake, *Geophys. Res. Lett.*, 39, L22305, doi:10.1029/2012GL053805.